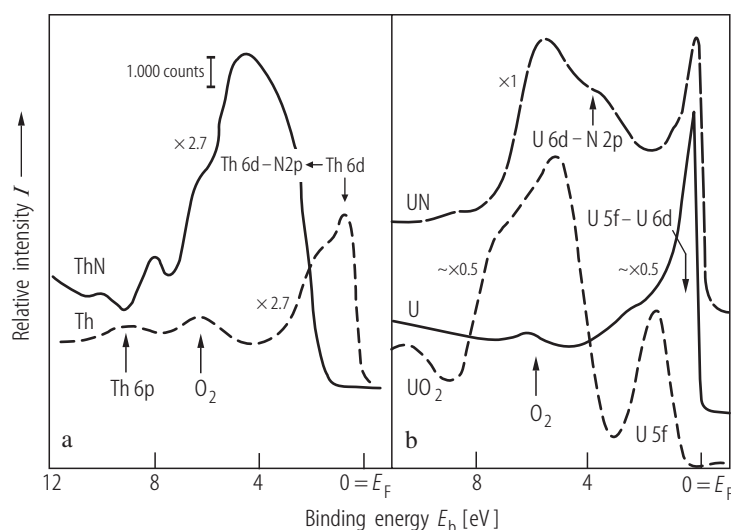
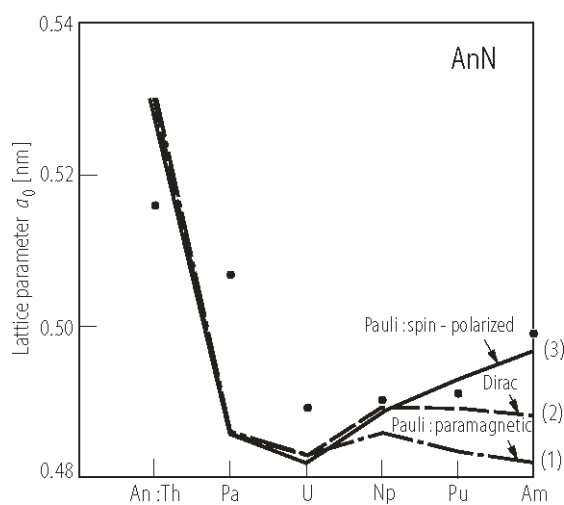


## II. AnN. Actinide mononitrides.



**Fig. II.1.** AnN (An = Th,U). Angle integrated valence band spectra ( $h\nu = 40.8$  eV) for (a) ThN compared to Th and for (b) UN s.c. compared to U metal [80NTCB]. A narrow peak, cut by  $E_F$  is identified as being of 5f-6d character in the case of U metal. The 6d electrons in ThN and UN are moved down to  $\sim 4$  eV to form chemical bonds with the N 2p electrons. Most of 5f electrons in UN remain near  $E_F$  while the 5f electrons in insulating  $UO_2$  (broken line) appear as a peak at 1.5 eV below  $E_F$ . Numbers by spectra are magnified numbers. Note that a comparison of the valence spectrum (a) of ThN with that presented in [02GHBW] yields serious difference showing rather a close similarity to that of  $Th_3N_4$ , being non-metallic in contrast to metallic ThN (see Fig. II.2).

For Fig. II.2 see next page



**Fig. II.3.** AnN. Lattice parameters of actinide nitrides calculated by (1) self-consistent LMTO, (2) RLMT0 and (3) LMTO spin-polarized methods, compared to the experimental lattice parameters (closed circles) [82B], [84B3]. Note that the calculated lattice parameters are improved by RLMT0 between NpN and AmN and for the latter the correct parameter is obtained when spin-polarized LMTO is used. The presented trend in lattice parameters is interpreted as being of metallic 5f-5f and covalent 5f-2p contributions to the equation of state (see Fig. I.18). Summary of principal results are gathered in the Table below.  $n_f$  is the partial actinide f occupation number,  $N_f(E_F)$  is the partial f-density of states at  $E_F$  (in states/Ry F.U.) and  $IN(E_F)$  is the Stoner product (see [82B]).

	ThN	PaN	UN	NpN	PuN	AmN
$n_f$	0.9	1.7	2.8	3.8	4.9	6.0
$N_f(E_F)^1$	7	11	88	174	100	209
$IN(E_F)$	0.09	0.18	1.8	3.6	1.9	3.8
$N_{f5/2}(E_F)^2$	1.8	9	66	370	69	2
$N_{f7/2}(E_F)$	2.2	4	6	27	5	1

<sup>1)</sup> LMTO and <sup>2)</sup> RLMT0.

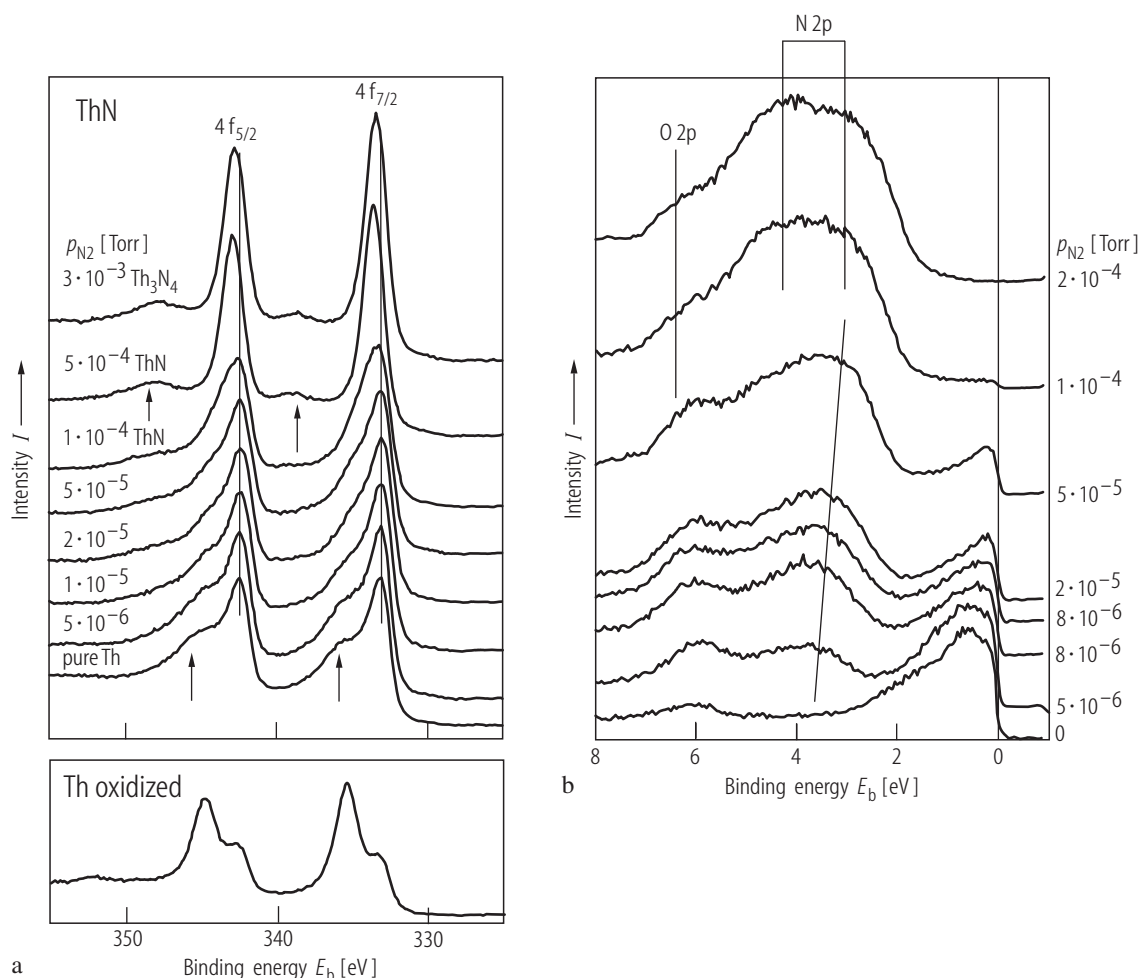


**Fig. II.2.** ThN, (thin films). **(a)** The 4f-core spectra of Th under varying nitrogen partial pressure (upper panel) [02GHBW]. The gradual nitrogenation of Th by increasing the  $N_2$ -partial pressure affects the 4f-core-level spectra by the formation of ThN (gold colour) for  $1 \cdot 10^{-4}$  Torr. At higher pressure X-ray analysis indicates the formation of  $Th_3N_4$  (copper colour). See weak satellites (arrows) due to the shake-up process, i.e. formation of a final state with higher energy. The lower panel showing the oxidized Th spectra is given for comparison with pure Th metal (the

lowest curve in the upper panel). **(b)** The HeII valence-band spectra of the Th–N system depending on the partial nitrogen pressure given in Torr [02GHBW]. The marked lines indicate the position of O 2p and N 2p spectral maxima. See that the second maximum at about 4.5 eV starts to dominate where non-metallic  $Th_3N_4$  is expected. The other feature, spread between  $E_b = 3$  and 4 eV, involves the N 2p states hybridized weakly with the 5f states, which show a small but not zero occupancy.

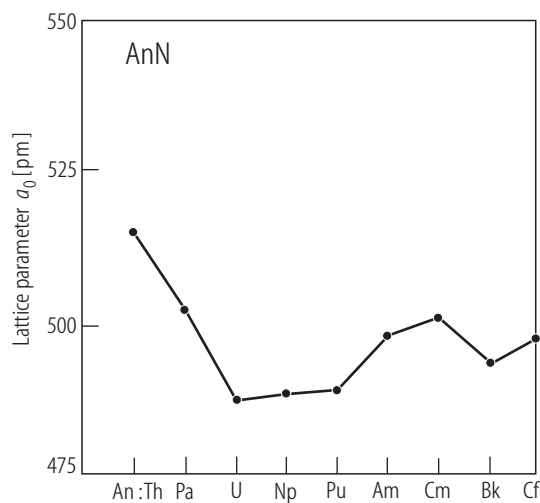


**Fig. II.4.** AnN. Lattice parameters,  $a_0$ , of actinide mononitrides [87B];  $a_0$  for CfN is from [86NMHP]. Note that the isomorphism of all the actinide mononitrides (they crystallize in the NaCl ( $B_1$ )-type structure) allows one to visualize the bond length variation simply in terms of the lattice parameters. As is the case of actinide metals from Pa to Pu, also for their mononitrides the bond shortening occurs.

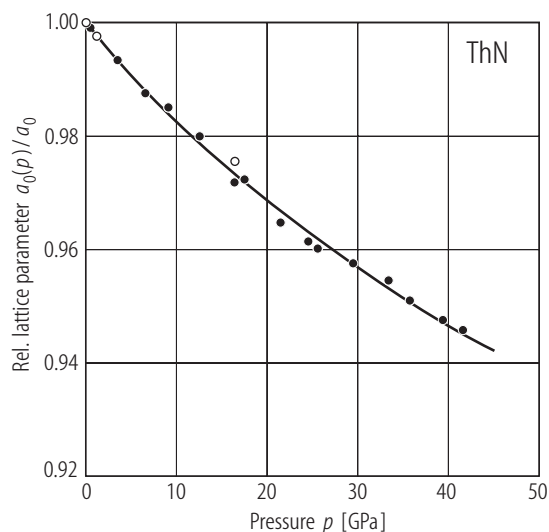
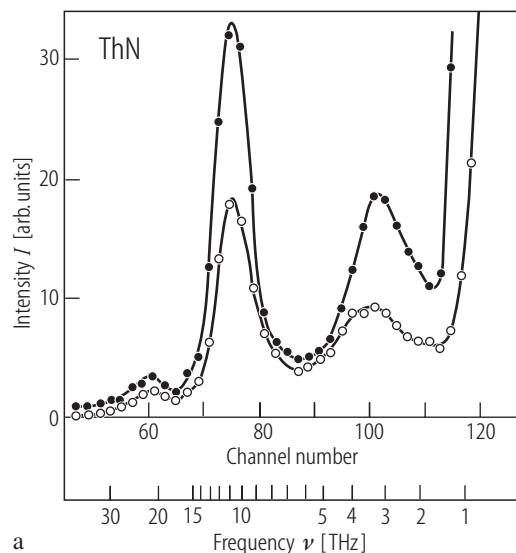
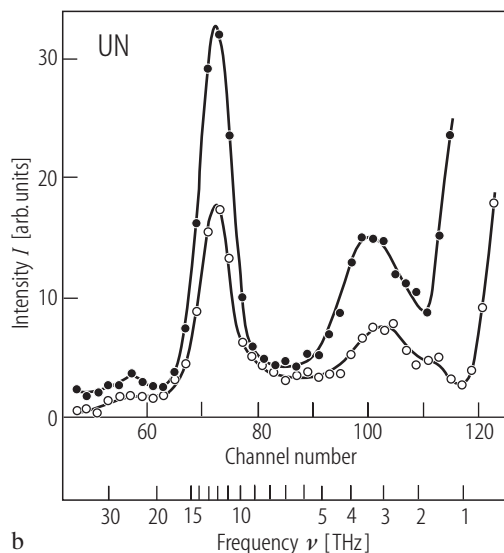


**Fig. II.5.** ThN. The lattice parameter ratio,  $a(p)/a_0$ , at RT vs. pressure up to 47 GPa [85GSBI].  $a_0 = 0.51666(4)$  nm. Open symbols denote data obtained in decreasing pressure. Solid curve is the fit to the Murnaghan equation with  $B_0 = 175(15)$  GPa and  $B_0' = 4.0(4)$ . In contrast to UN [85SGB], no structural phase transition was found.



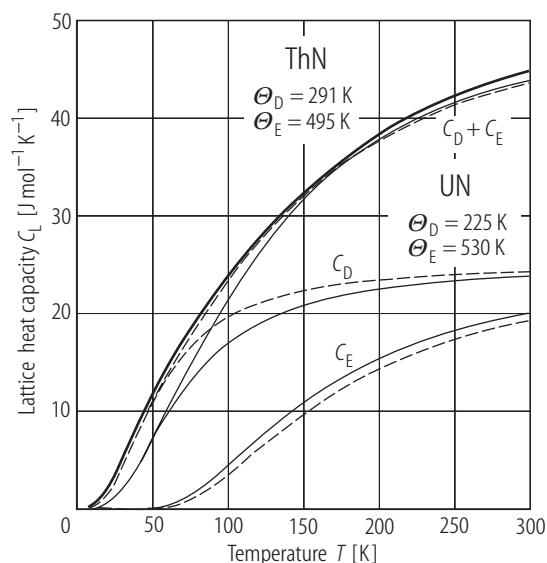
a



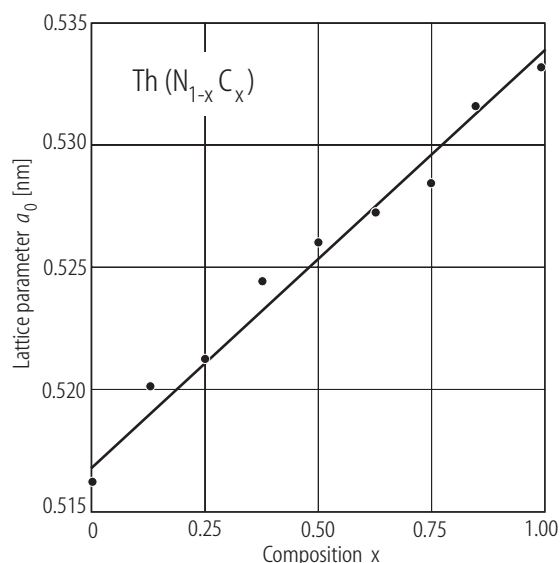
b

**Fig. II.6.** ThN, UN. The time-of-flight spectra using 2 Å incident neutrons for (a) ThN and (b) UN measured for two scattering angles 17° (open circles) and 63° (closed circles) [74W]. A mean optical frequency is 10.3 and 11.8 THz for ThN and UN, respectively. The 3 Å run for UN gives a

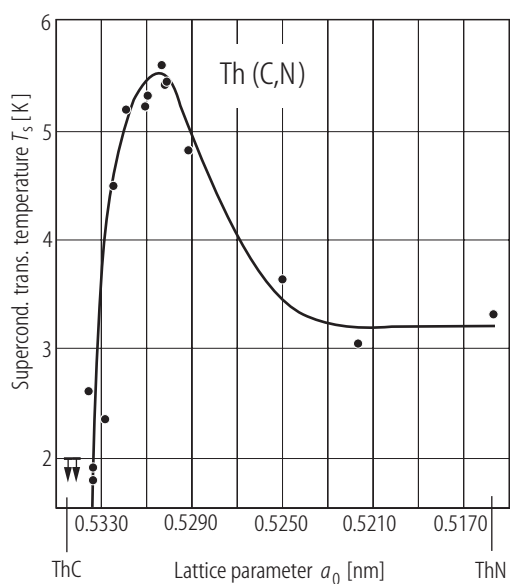
spectrum similar to that of UC (Fig. I.12) with acoustic peak at 3.4 THz and optic one at 11.8 THz, which makes very similar phonon dispersion curves for UC and UN (compare Fig. I.30 and Fig. II.33, respectively).



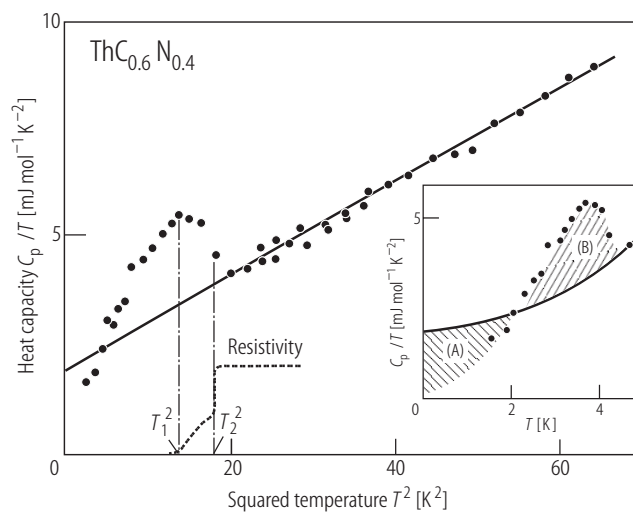
**Fig. II.7.** ThN (UN). Summary of the lattice heat capacity contributions,  $C_L$ , to UN, based on the data obtained for ThN by [72DDD] (thick-line curve) (Fig. II.69a). The solid line and dashed line give both the Debye and Einstein contributions reported by [72DDD] and [90YS] (Fig. II.70), respectively. Note a good fit in the case of the latter work.



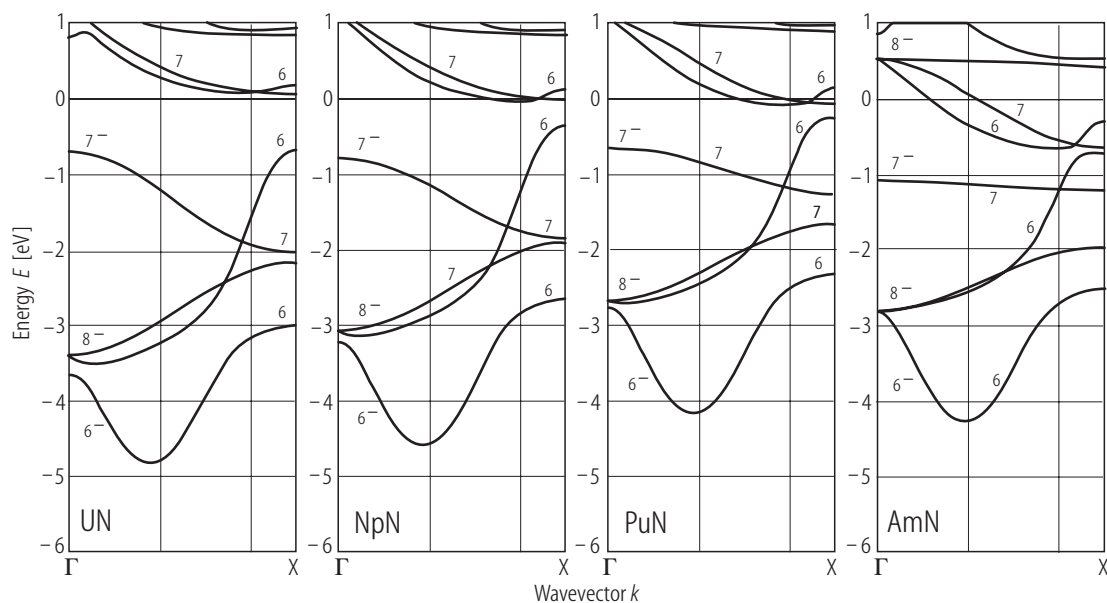
**Fig. II.8.**  $\text{Th}(\text{C}_x\text{N})$ . The lattice parameters,  $a_0$ , of the solid solutions  $\text{ThN}_{1-x}\text{C}_x$  (where  $0 \leq x \leq 1.0$ ) as a function of the carbon concentration  $x$  [63SW]. Note that Vegard's law is obeyed.



**Fig. II.9.**  $\text{Th}(\text{C}_x\text{N})$ . The variation of  $T_S$  vs. lattice parameter,  $a_0$ , for the complete solid solutions  $\text{Th}(\text{C}_{1-x}\text{N}_x)$  [72GSK]. The maximum of  $T_S$  occurs for VEC between 3.8 and 3.9 per atom.

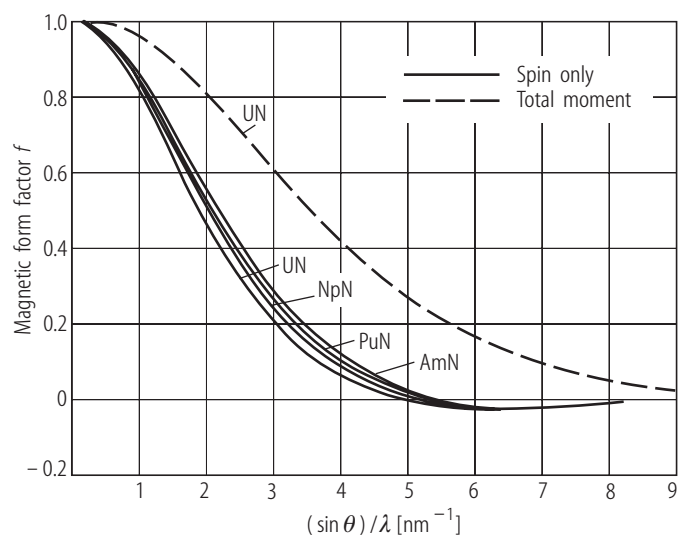


**Fig. II.10.**  $\text{Th}(\text{C}_x\text{N})$ . The  $C_p/T$  vs.  $T^2$  plot for  $\text{ThC}_{0.6}\text{N}_{0.4}$  [79MBA].  $\gamma(0) = 1.9 \text{ mJ/mol K}^2$ . The inset shows  $C_p/T$  vs.  $T$ . Note at  $T_S = 3.8 \text{ K}$  the occurrence of superconductivity. In the inset the areas A and B on each side of the curve  $\gamma(0) + \beta T^2$  (solid line) are equal to each other according to theoretical prediction.

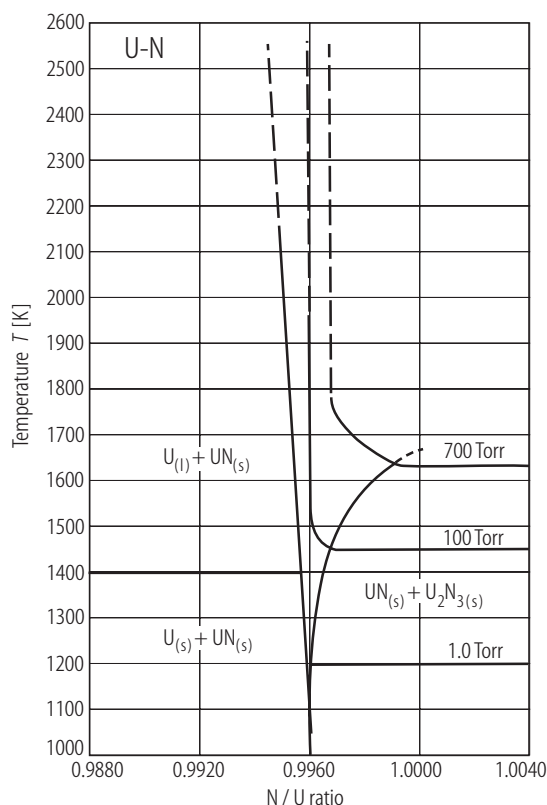


**Fig. II.11.** AnN (An = U...Am). Energy bands calculated along the  $\Gamma X$  direction with RLMT0 method [84B3]. Note that the number of distinguishable bands along lines increases since only double degeneracy remains away from the  $\Gamma$  point. So the labeling is in terms of double group

notation. The magnitude of the spin-orbit splitting of the VB states approaches several eV near X. As was found in the LMTO calculations, no distinct changes in valence band composition are noticed across the series (not shown).

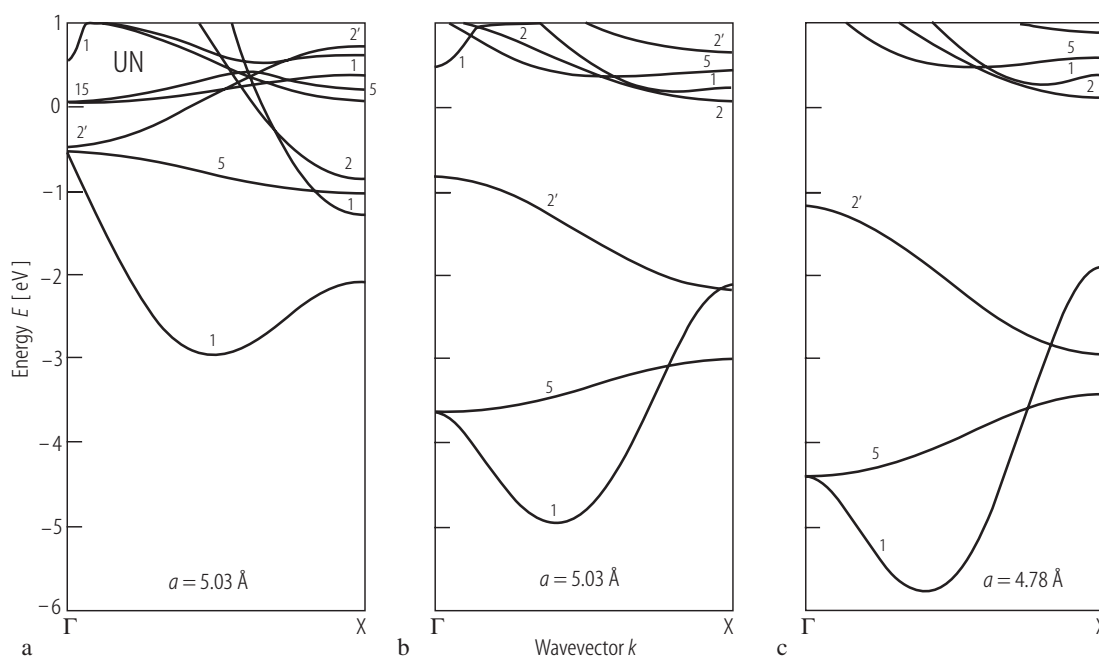


**Fig. II.12.** AnN (An = U...Am). Magnetic form factor of AnN mononitrides. The difference between calculated magnetic form factors of the spin-only densities (solid lines) and the experimental one for UN [65C], which is identical to the calculated magnetic form factor of UN with including an orbital moment (dashed line) [83BK]. It means that spin-orbit coupling induces a predominant orbital magnetic moment ( $-1.5 \mu_B$ ) antiparallel to the spin moment ( $1.0 \mu_B$ ) in the spin-polarized energy bands.

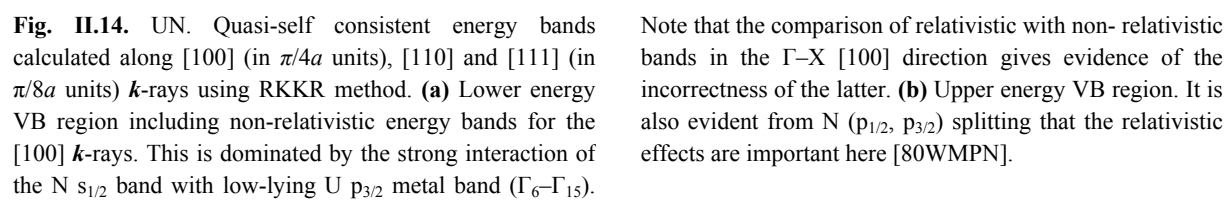


**Fig. II.13.** UN. The partial U–N phase diagram around  $\text{UN}_{0.996}$  [71H]. UN has a very narrow composition linearity between  $\text{UN}_{0.985-0.997}$ , in agreement with [70BBB]. Boundary phase compositions were established in vacuum and at 1, 100, and 700 Torr (see also phase equilibria in the U–N system [66BB]).

For Fig. II.14 see next page



**Fig. II.15.** UN. Self consistent LMTO in ASA band structures: energy bands along the  $\Gamma\text{X}$  direction [84B1]. **(a)** The unhybridized or pure bands in the NaCl-type compounds, namely s-state ( $\Gamma_1$ ), p-states ( $\Gamma_{15}(3)$ ), f-states ( $\Gamma_{2'}(1)$ ,  $\Gamma_{15}(3)$ ,  $\Gamma_{25}(3)$ ) and d-states ( $\Gamma_{25}(3)$ ,  $\Gamma_{12}(2)$ ), all at the  $\Gamma$  point. In brackets a degeneracy is given. **(b)** hybridized bands, close to the equilibrium lattice parameters (see the foot of the figures). **(c)** hybridized bands under pressure. For details see the original paper. Similar energy band variations are also presented for UC and UO.



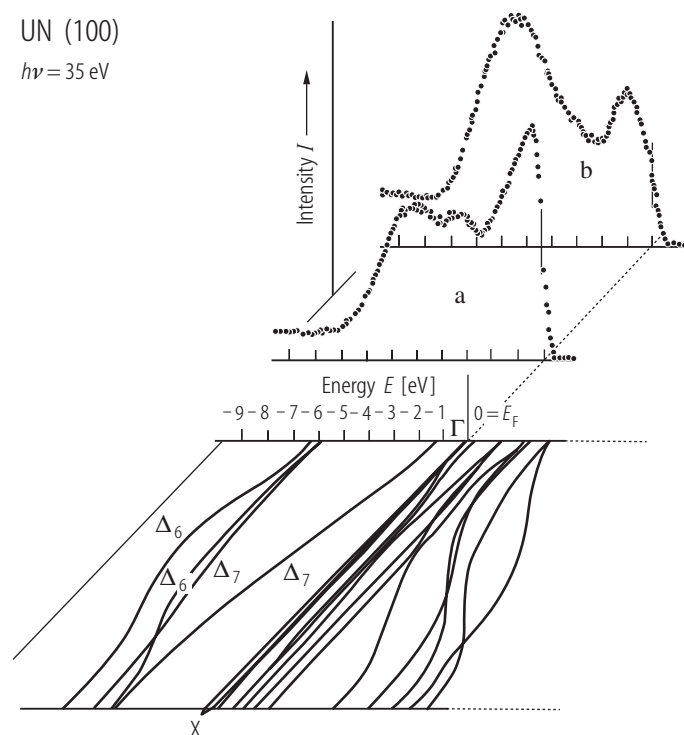


**Fig. II.16.** UN. Band structure along  $\Gamma$  to X [80WMPN], [83BCCH], compared to the results of normal photoemission [82B1] from the UN (001) surface with (a) s and (b) p polarization. Note a consistence between both presentations [87WG].

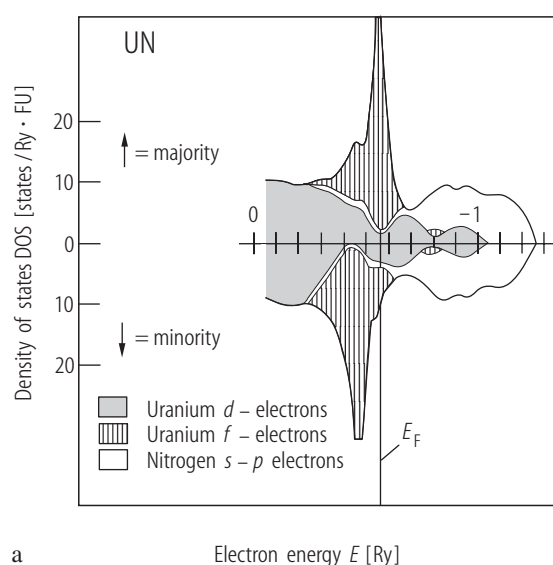
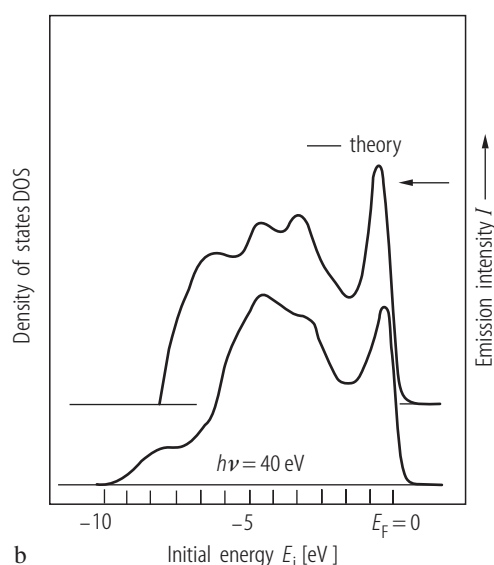


**Fig. II.17.** UN, UN s.c. (a) Electronic densities of states calculated by a self-consistent cellular multiple scattering (CMS) technique for a finite cluster in condensed-matter-like boundary conditions [79EK2], [79KE]. The hatched and shaded areas represent the amount of f and d character, respectively, for spin up (majority) and down (minority). No correlations other than exchange were used for the f electrons. The s- and p-bands extend beyond  $E_F$ . Note that



DOS for minority spin is predominantly of U d character and that for majority spin of U f character, as if the d electrons were polarized against the f - moment. There the theoretical results are in agreement with the optical DOS as obtained by EDC's for photoemitted electrons near  $E_F$  at  $h\nu = 40 \text{ eV}$ . (b) Theoretical total DOS found from the band structure calculation of figure (a) is compared with the experimental EDC's taken at  $h\nu = 40 \text{ eV}$  [79EK2].



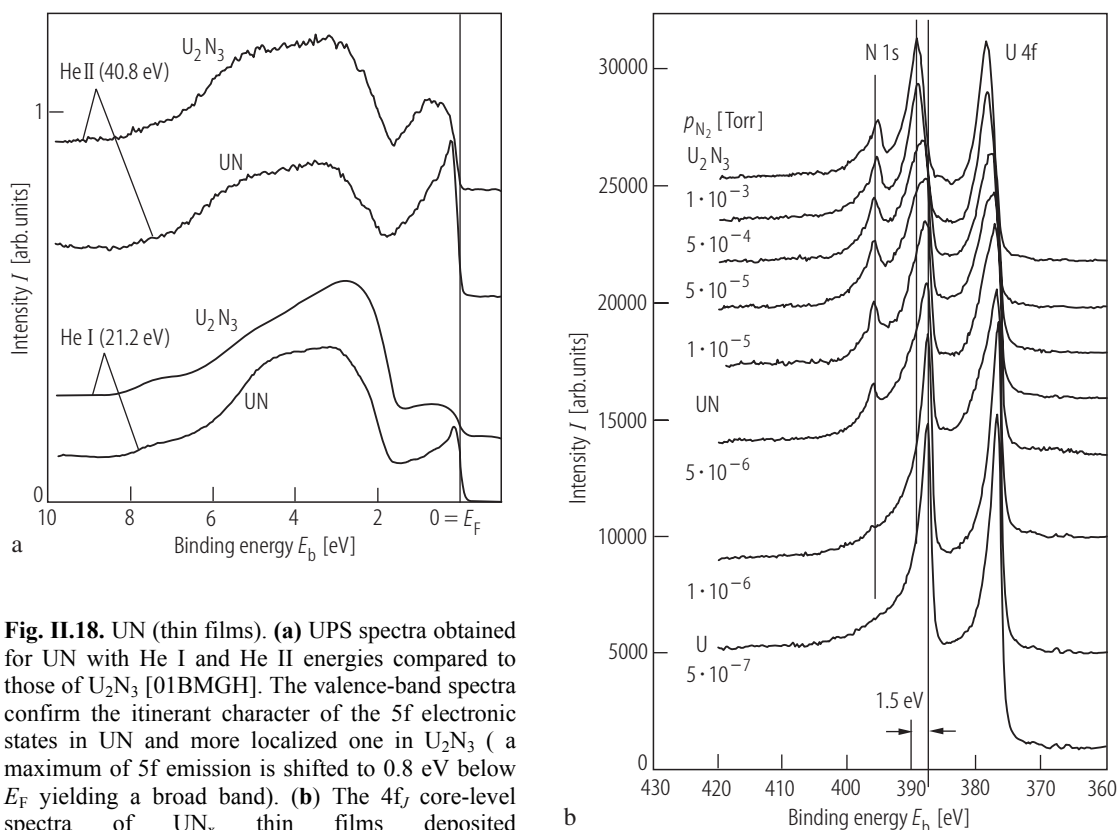


**Fig. II.18.** UN (thin films). **(a)** UPS spectra obtained for UN with He I and He II energies compared to those of  $U_2N_3$  [01BMGH]. The valence-band spectra confirm the itinerant character of the 5f electronic states in UN and more localized one in  $U_2N_3$  (a maximum of 5f emission is shifted to 0.8 eV below  $E_F$  yielding a broad band). **(b)** The  $4f$  core-level spectra of  $UN_x$  thin films deposited at RT with increasing  $N_2$  partial pressure in the sputter gas [01BMGH]. The stoichiometric UN is formed at  $5 \cdot 10^{-6}$  Torr of  $N_2$  partial pressure. Note that the spin-orbit lines remains asymmetrical indicating a high DOS at  $E_F$ . Further increase of the  $N_2$  partial pressure results in more symmetric  $4f$ -lines due to the formation of  $U_2N_3$  with an apparent lower DOS and with BE shifts by 1.5 eV to higher energy. For real structure and magnetic properties of UN films see [05RHKW]. It was shown that increasing disorder (low-temperature deposition conditions for obtaining thin films) suppresses the long-range antiferro-magnetism and induce a ferromagnetic component in exchange interactions, leading to a cluster glass type of magnetic ordering at low temperatures.

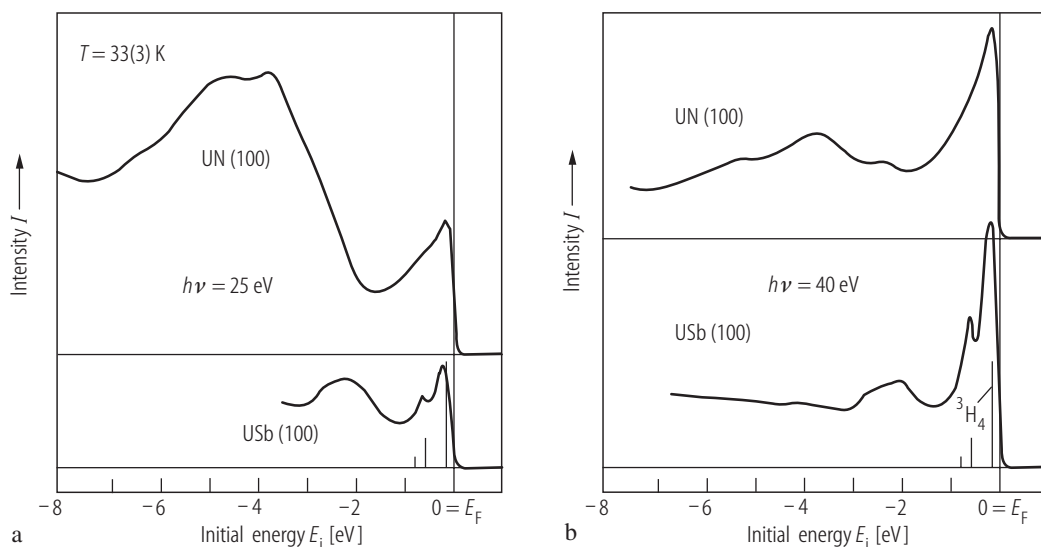


**Fig. II.19.** UN s.c. Angle integrated EDC's taken with photon energies  $h\nu = 25$  **(a)** and 40 eV **(b)**, compared to those of USb [83RHH]. The bar diagram describes an  $f^2$  final-state multiplet. One notes a big difference between UN and USb. A single 5f emission is significantly wider than that of isoelectronic USb [see 82RMV].

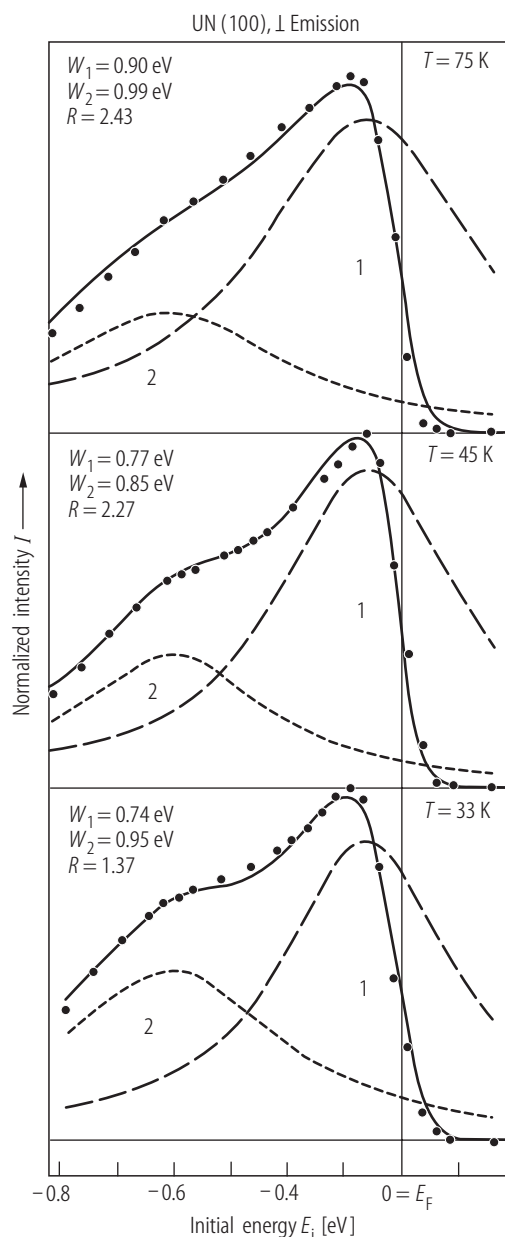
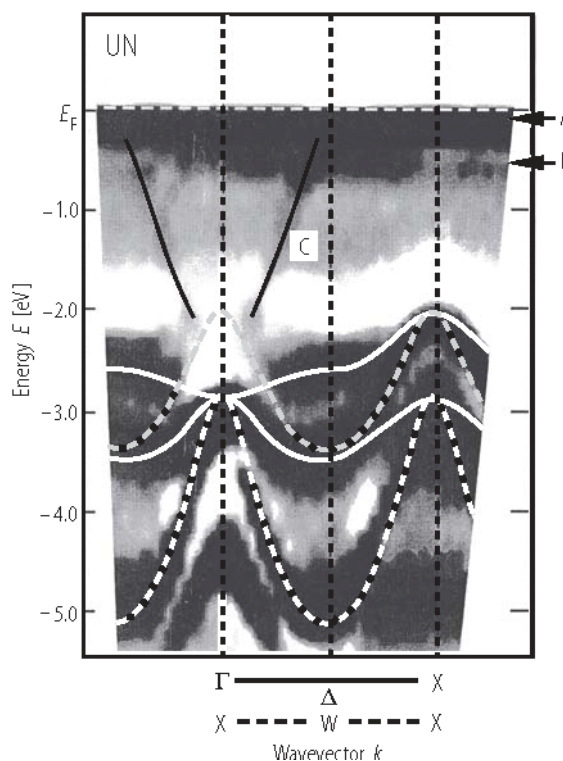
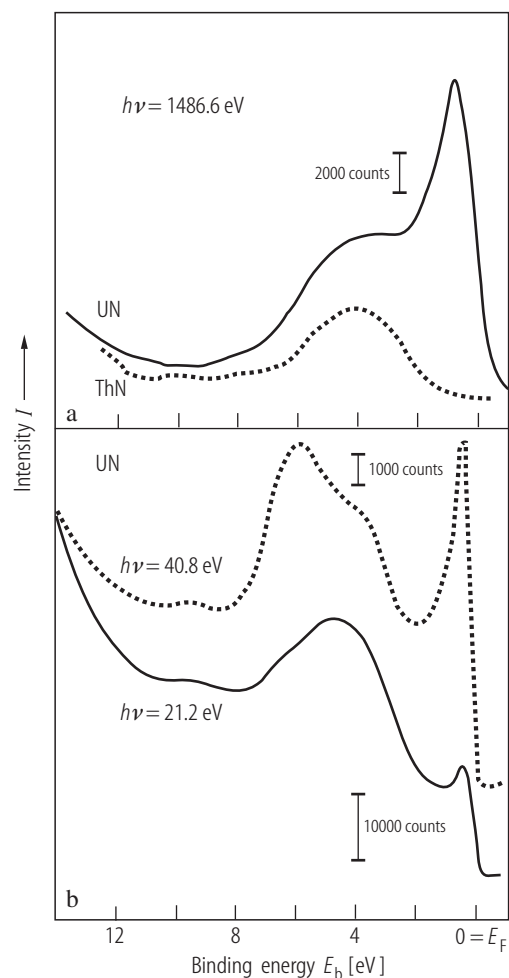


**Fig. II.20.** UN s.c. Angle resolved EDC's taken at three different temperatures as indicated, at  $h\nu = 25$  eV [83RHH]. The black circles are experimental results after background subtraction. Solid lines indicate the theoretical functions composed of two Lorentzians containing peak 1 ( $-0.09$  eV) and peak 2 ( $-0.78$  eV) with intensities  $I_1$  and  $I_2$  having widths  $W_1$  and  $W_2$ , respectively. The intensity ratio  $R = I_1 W_1 / I_2 W_2$ .

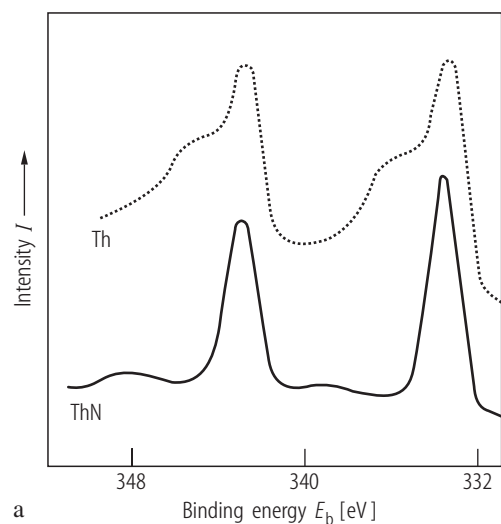


**II.22.** UN s.c. The “experimental band structure” found from high-resolution ARPES measurements [01IKST], compared with the band structure calculations based on the itinerant U 5f-electron model (H. Yamagami, unpublished) (solid and broken white lines and the solid black line), respectively. The completely occupied VB consists of nitride p-states while the electronic structure near  $E_F$  is due mainly to the U 5f states hybridized with the U 6d-states. However, despite the highly dispersive latter bands predicted by calculation, in the very vicinity of  $E_F$  there exist two non-dispersive bands of mainly 5f-character labeled by letters A and B, as in the case of USb. They are explained [01IKST] as the U  $5f^2$ -final state multiplet of trivalent  $U^{3+}$ , indicating rather localized nature of U 5f-electrons. Nevertheless, the observation of relatively larger intensity of the peak A in UN than in USb and its closer location to  $E_F$ , makes a more itinerant character of U 5f-electrons (considerably larger  $\gamma(0)$ -value) in the uranium nitride than in the uranium antimonide. These observations are consistent with a dual character of 5f-electrons in the uranium mononitrides (see the Introduction). The band C, represented by the gray area, shows a flat band with a small dispersive structure determined in calculations based on the itinerant U 5f model (H. Yamagami, unpublished).

For Fig. II.21 see next page



A



B

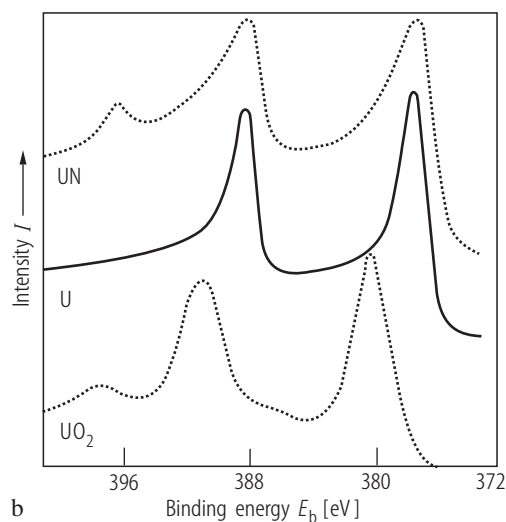


**Fig. II.21.** UN s.c. (ThN). **(A)** Valence-band XPE spectra at different photon energies **(a)** at 1486.6 eV for ThN (rather Th<sub>3</sub>N<sub>4</sub>-see Fig. II.1) and UN, **(b)** at 21.2 and 40.8 eV for UN [80NTCB]. For both compounds the 6d density is largely removed from  $E_F$ . For UN the sharp peak located close to  $E_F$  is predominantly of 5f character. As a prove of the latter is a dramatic increase of the intensity as the photon energy increases. **(B)** 4f-core level XPE spectra ( $h\nu = 1486.6$  eV) **(a)** ThN (Th<sub>3</sub>N<sub>4</sub>) compared to Th metal spectra and **(b)** UN s.c. compared to U metal and UO<sub>2</sub> spectra [80NTCB]. Note that the linewidth of UN (4.6 eV) is  $\sim 2.5$  times larger than that in U metal and is asymmetric like for U-metal. The energy of a shake-up from the Th 6d level is increased by  $\sim 4$  eV over that observed in Th metal. In contrast to UN, the linewidth of the 4f lines in ThN is  $\sim 1.6$  eV and is quite symmetric. The latter spectra resembling rather those of Th<sub>3</sub>N<sub>4</sub> in paper by [02GHBW]. The anomalously broad 4f core levels in UN are explained in terms of energy-loss mechanisms or alternating valence.

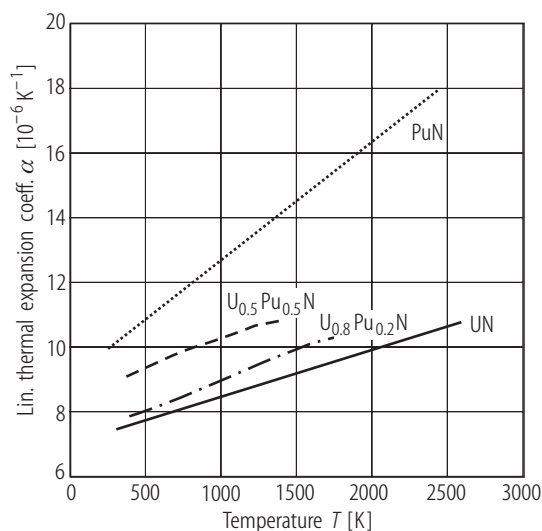
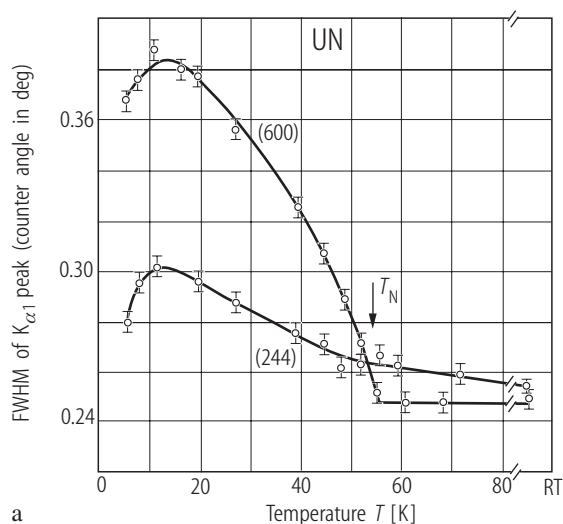
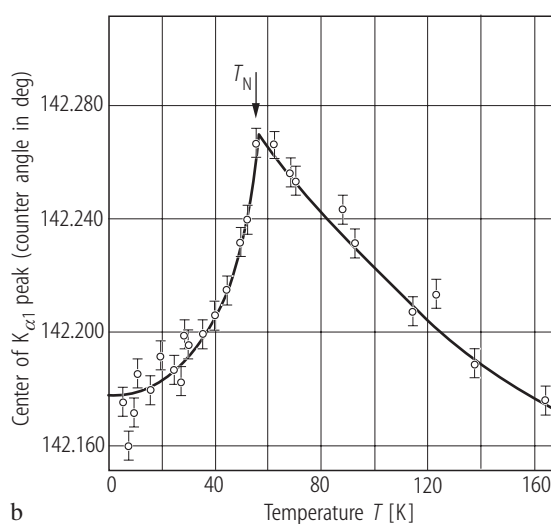


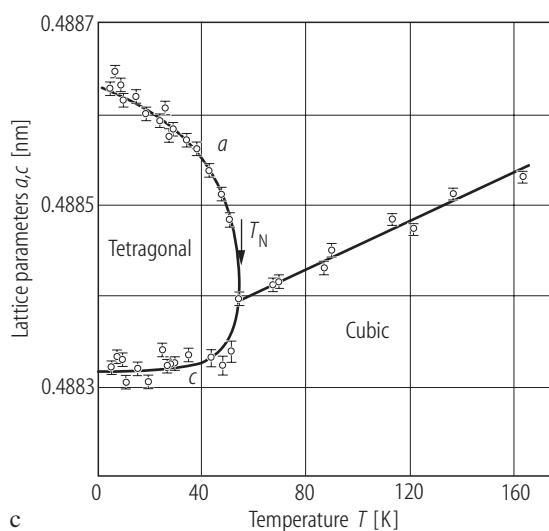
**Fig. II.23.** AnN. (An = U, Pu). Linear thermal expansion coefficient,  $\alpha$ , vs.  $T$  for UN, PuN, estimated between 300 and about 2600 K as well as for the solid solutions  $U_{0.8}Pu_{0.2}N$  and  $U_{0.5}Pu_{0.5}N$ . The data of different authors were compiled by [98SA]. No information exists for NpN.



a



b



c

**Fig. II.24.** UN s.c. Single crystal X-ray diffractometry [75MSWK]: **(a)** The widths of reflections (600) and (244) vs. temperature  $T$ . Note that below  $T_N$  a broadening of these reflections occurs, with much more effect for (600). The difference in the intensities (3:1, respectively) of these two reflections, confirms existence of a tetragonal distortion at  $T_N$  (= 55(2) K). **(b)** The center position (counter angle) of the (600)  $K_{\alpha 1}$  peak vs.  $T$ . This effect is caused by the irregular volume change of the cell at  $T_N$ . The effect was observed also in the powder work (Fig. II.25) [70M]. **(c)** Lattice parameters  $a$ ,  $c$  vs.  $T$ , calculated by combining the  $d$ -spacing found from the line width with the mean lattice parameter. For arguments about the lack of tetragonal distortion in UN see Fig. II.26 and Fig. II.27.

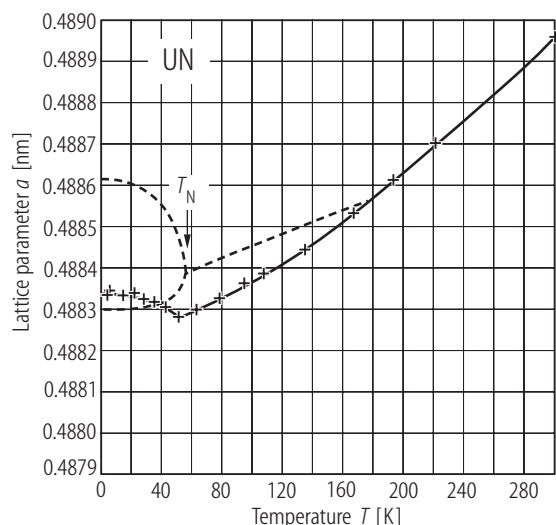


**Fig. II.25.** UN. Lattice parameter,  $a$ , vs. temperature,  $T$ , in the range 4...300 K measured on powder (solid line and symbols) [70M]. Schematically is also shown (dashed line) a tetragonal distortion below  $T_N$  and a linear behaviour above  $T_N$  up to 160 K, reported by [75MSWK] on single crystals. See ref. [80KLMV] and Fig. II.27 discussing the presence in UN of a maximum distortion of  $\delta \approx 3 \cdot 10^{-4}$ , which cannot be detected by X-ray measurements

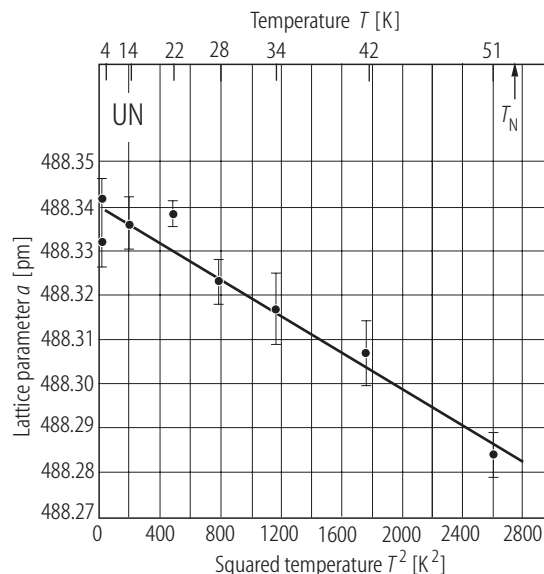


**Fig. II.28.** UN. The lattice parameter,  $a$ , below the Néel temperature ( $T_N = 52$  K) plotted against  $T^2$  [70M]. This yields that the temperature dependence of  $a(T)$  and the expansion coefficient  $\alpha(T)$  can be expressed in the ordered state as:  $a(T) = [4.88340(2)] - [2.05(15)] \cdot 10^{-7} T^2$  (Å) and  $\alpha(T) = -[8.4(6)] \cdot 10^{-8}$ . Note that UN has a negative expansion coefficient below  $T_N$ .

For Fig. II.27 see next page

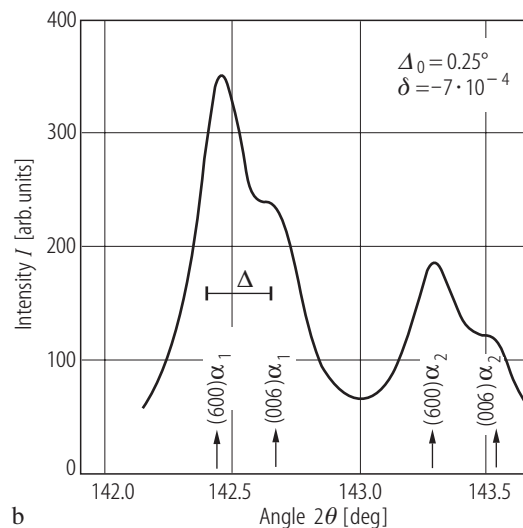
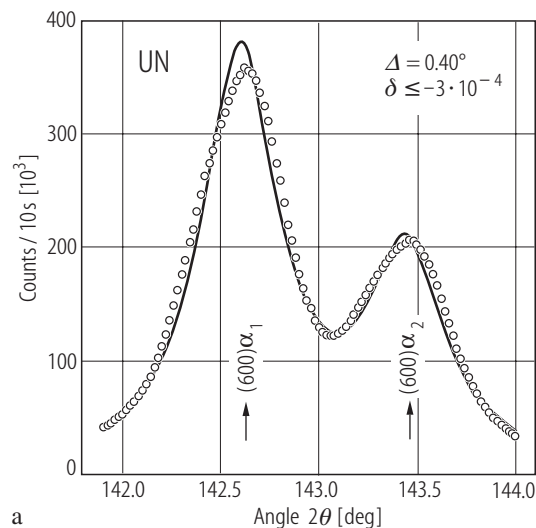


**Fig. II.26.** UN s.c. (100). **(a)** Diffraction profile of the (600) reflection, taken at 5.25 K with Cu  $K_\alpha$  radiation by means of Bond's technique [80KLMV]. The open circles are experimental points, while solid line is the theoretical fit. **(b)** Simulated (600) diffraction reflection with the parameters given in [75MSWK]. In contrast to the

observation, the profiles of peaks with such a tetragonal distortion  $\delta$  ( $= -7 \cdot 10^{-4}$ , as shown in figure **(b)**), should lead to marked asymmetry, and doesn't follow the parabolic regime shown in Fig. II.27. It means that the line broadening is a result of internal strains rather than the tetragonal distortion.  $\Delta$ ,  $\Delta_0$ : see Fig. II.27.

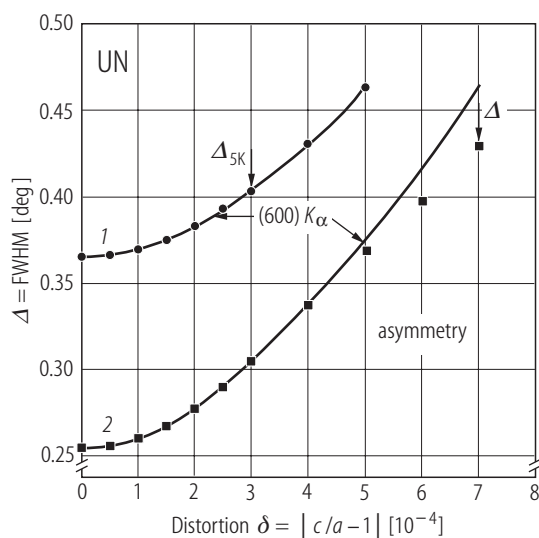


**Fig. II.27.** UN s.c. (100). The full width at half maximum (FWHM)  $\Delta$  vs. the simulated tetragonal distortion  $\delta (= c/a - 1)$  in the magnetically ordered state [80KLMV]. The intrinsic half-width  $\Delta_0$  is  $\Delta$  at  $\delta=0$ , corresponding to the high-temperature normal state. The data 1) and 2) correspond to the results obtained in [80KLMV] and [75MSWK], respectively. The difference in  $\Delta_0$  for both these cases is due to different single crystals used. The solid line is a fit to the equation:  $\Delta^2 = \Delta_0^2 + c\delta^2$ , where  $c$  is constant. For larger  $|\delta| (\geq 4 \cdot 10^{-4})$  the peak (600) should become asymmetric like in Fig. II.26b and in such a situation the experimental points are expected to deviate from the solid line. So that for  $\Delta_{5K} = 0.40^\circ$ ,  $\delta \leq 3 \cdot 10^{-4}$ , i.e. a value being close to the maximum possible tetragonal distortion, usually unable to detect in the case of not observed asymmetry (see Fig. II.26a) in both experiments [80KLMV] and [75MSWK]. This means that the distortion of the UN unit cell below  $T_N$  reported in [75MSWK] and schematically shown in Fig. II.25 should practically not be observed.

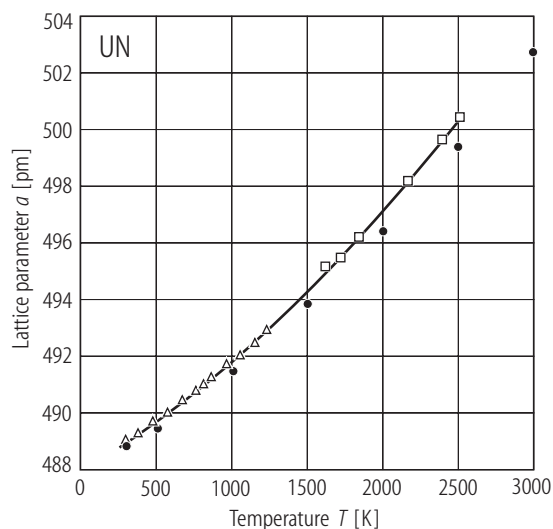


**Fig. II.30.** UN. Lattice parameter,  $a$ , vs.  $T$  from room temperature up to 2593 K, based on the data reported by [59KE] (open triangles) and [70BBB] (open squares) and correlated by [90HTP1] (solid line) with the equation:  $a(T) = 487.9 + 3.264 \cdot 10^{-5} T + 6.889 \cdot 10^{-9} T^2$  [pm]. The change in the lattice parameter with temperature (closed circles) was obtained by MD calculations [00KYYU1] using the interatomic potential function for U – N interaction proposed by [76I].

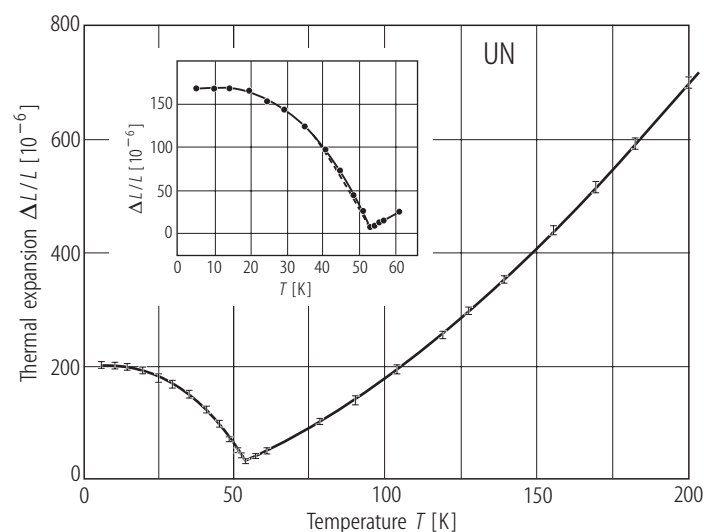
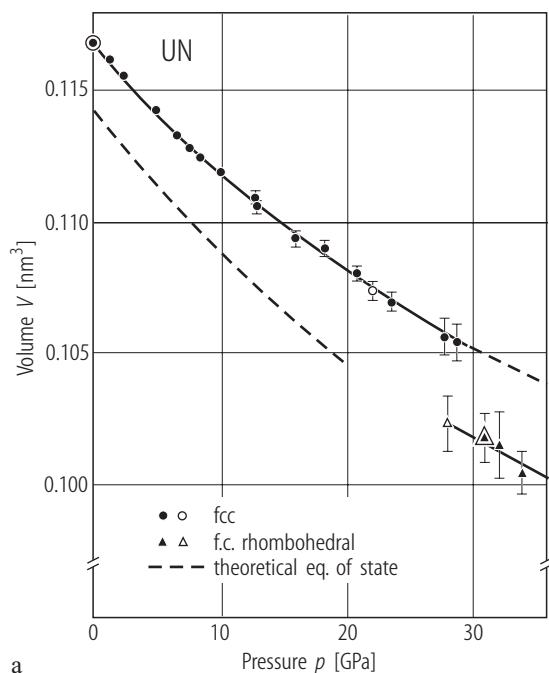


**Fig. II.29.** UN s.c. The thermal expansion,  $\Delta L/L$ , vs. temperature,  $T$ , along the three equivalent [100] axes [77VD2]. All the three results found at all temperatures measured fall within the indicated bars which implies an equal single- $k$  domain distribution. As shown in the inset, the strain due to magnetic ordering (closed points) scales well to the square of the sublattice magnetization, taken from [65C] (dashed line).  $T_N = 53$  K.



a

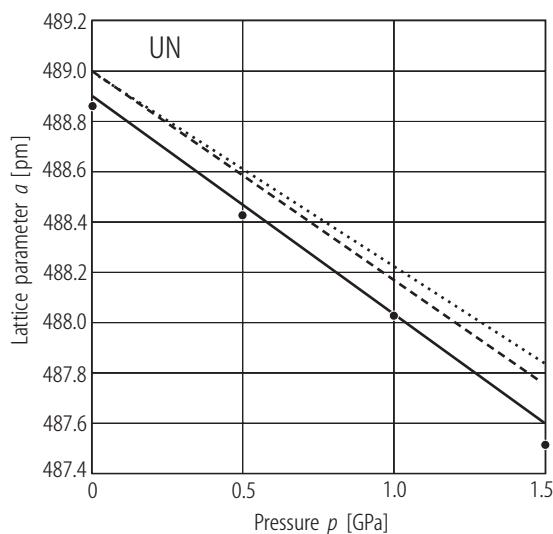
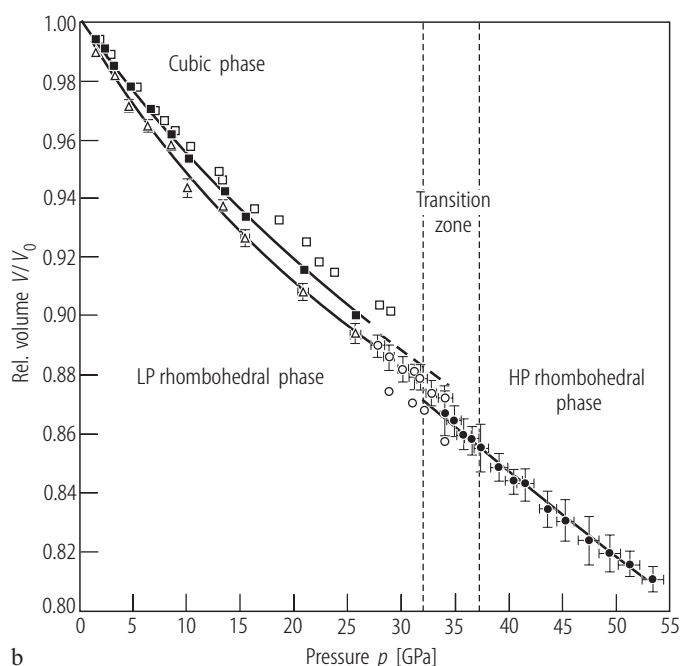


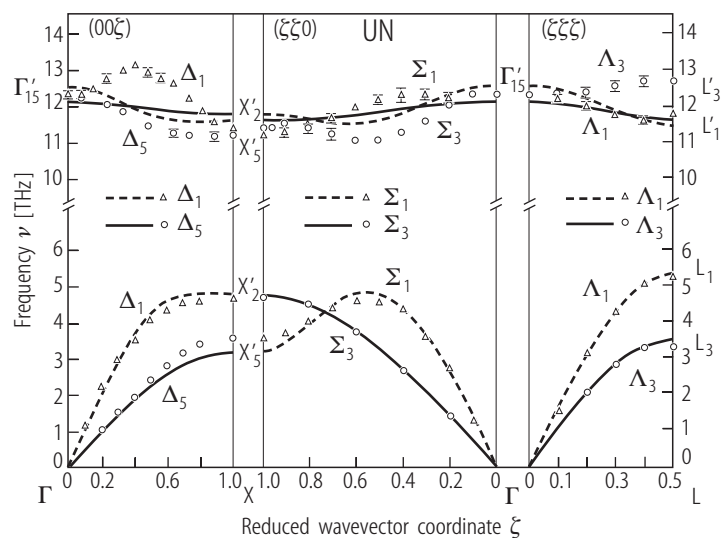
**Fig. II.32.** UN. Lattice parameter,  $a$ , calculated (by the MD method) vs. pressure,  $p$ , up to 1.5 GPa (closed circles) [00KYYU1], compared to the experimental data: [90HTP1] (solid line), [69PD] (dashed line), and [72GC] (dotted line).



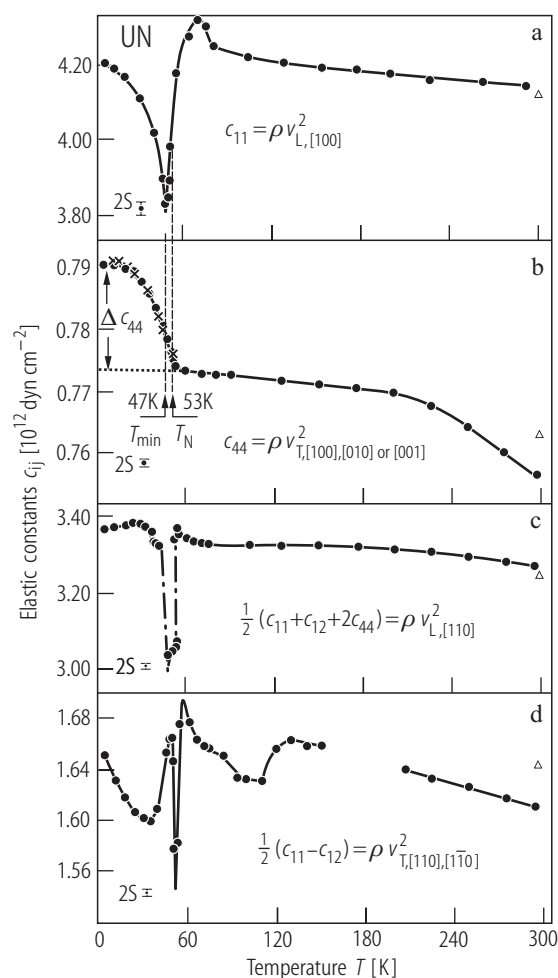
b

**Fig. II.31.** UN. (a) Unit cell volume,  $V$ , vs. pressure up to 34 GPa [85SGB]. Circles denote the f.c. cubic NaCl type phase stable up to 29 GPa, while triangles the high pressure, face centered, rhombohedral phase with  $a = 0.4657(5)$  nm and  $\alpha = 85.8(2)^\circ$  at 34 GPa. Open symbols are data obtained in decreasing pressure. There is a 3.2 % volume decrease at the 29 GPa first order transition. The solid curve for the cubic phase is the fit to the Murnaghan equation, using  $B_0 = 203(6)$  GPa and  $B'_0 = 6.3(6)$  (see also the similar data obtained from ultrasonic [70PGD] and from elastic constants [72GC] measurements). The dashed line is the calculated equation of state for UN [80BG1]. (b) Relative volume,  $V/V_0$ , vs.  $p$  up to 54 GPa [03LIH]. It appears that UN fcc structure (closed squares) transforms to a distorted low-pressure rhombohedral R3m structure before applying of pressure (triangles) owing to grinding the sample. This phase is stable up to 13 GPa. The complete transition takes place at 28 GPa. At 34 GPa it changes into a second high-pressure phase being the f.c. rhombohedral R3m structure. Open squares and triangles are data of figure (a). Lines are the results of Birch-Murnaghan fits to the experimental data. For bulk moduli see the Table below:

Phase	$B_0$ [GPa]	$B'_0$
Cubic phase	194(2)	4.5(2)
High-pressure rhombohedral phase	197(2)	2.6(2)



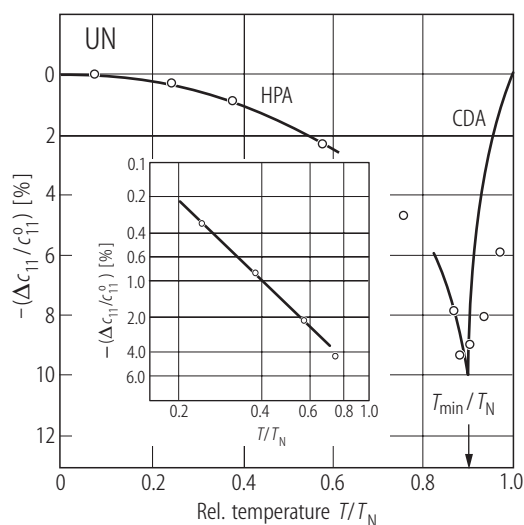
**Fig. II.33.** UN. Phonon dispersion relation for normal modes at 4.2 K [78DHSB]. A shell model involving radial and transverse nearest and next nearest neighbour force constants and the ionic charge was fitted to the data by solid (transverse) and dashed (longitudinal) lines. The results could be fitted by the rigid ion model (RIM) as well, but the overall goodness of the fit was unsatisfactory ( $\chi \approx 5.6$ ).



**Fig. II.34.** UN s.c. Elastic constants,  $c_{ij}$ , and their combinations vs. temperature,  $T$ , (closed circles) as determined from longitudinal (L) and transverse (T) ultrasonic velocities along main crystallographic directions [77VD1]. Room temperature values by [72GC] are marked by open triangles. (a)  $c_{11}$  vs  $T$ . Note a pronounced softening of 10% at 47 K (6 K below  $T_N = 53$  K). Such a difference between the temperature of longitudinal velocity minimum ( $T_{\min}$ ) and transition temperature ( $T_N$ ) were reported for MnTe and the rare earths. This behaviour is related to the presence or absence of first order spin-phonon coupling [77LV]. Except in  $c_{11}$  both first and second order interactions are also present in the longitudinal mode [ $\frac{1}{2}(c_{11}+c_{12}+2c_{44})$ ] and the shear mode [ $\frac{1}{2}(c_{11}-c_{12})$ ] (see Figs. (c) and (d)). (b)  $c_{44}$  vs  $T$ .  $c_{44}$  shows no anomaly below  $T_N$  where only second order interactions are present (see ref. [77LV] and Fig. II.35.). The difference  $\Delta c_{44}$  between the renormalized (closed circles) and unrenormalized values (dotted line) closely follows a dependence on the square of the sublattice magnetization  $m$  (crosses) [79L] (see also Fig. II.36).

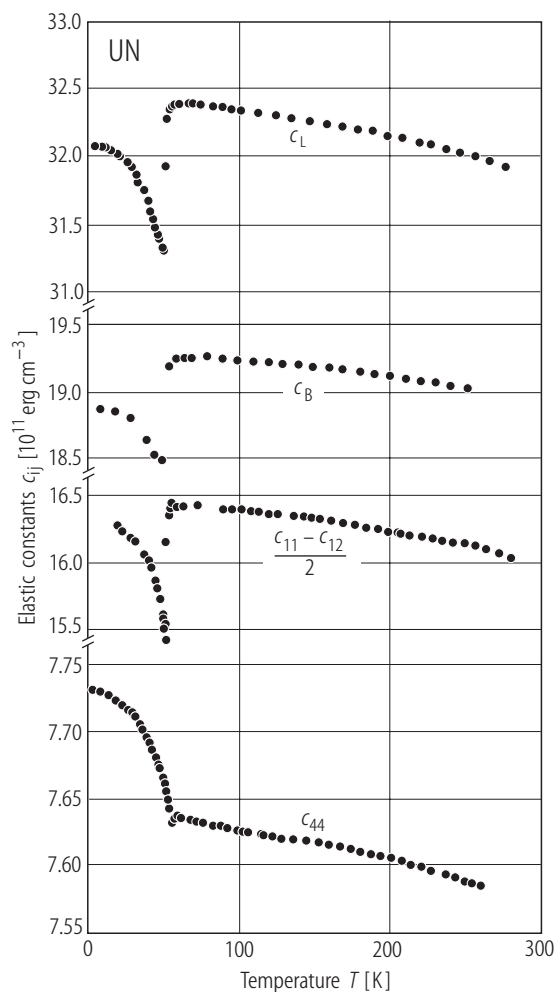
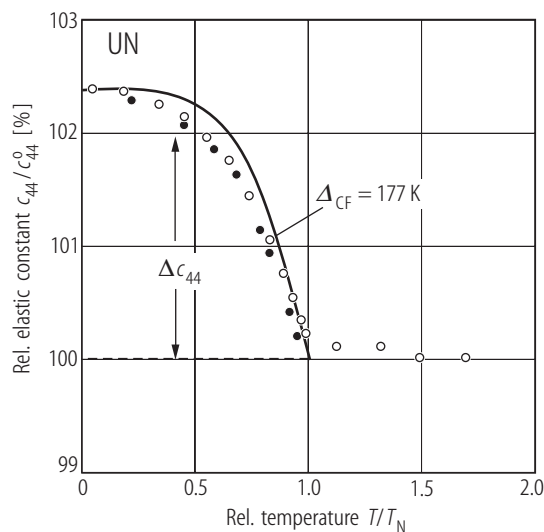


**Fig. II.36.** UN s.c. A comparison of the acoustic data (taken from 77VD1) normalized to 100 % of  $c_{44}^0$  at  $T_N$  ( $= 0.77 \cdot 10^{12}$  erg/cm<sup>3</sup>) (open circles) and neutron scattering data (taken from [65C]) (closed circles) in the form of the square of the sublattice magnetization  $m^2$  of UN [79L]. The measured and calculated values of  $m^2$  were adjusted to agree with normalized  $c_{44}$ . The solid curve is a calculation of  $m^2$  using a two-level model of ref. [78LL2] with a gap  $\Delta_{CF} = 177$  K. Thus, this model considers phonons in a lattice of ions described by two singlet status only.



**Fig. II.35.** UN s.c. Comparison of the experimental data presented as the ratio  $[\Delta c_{11}/c_{11}^0]$  (taken from [77DV] – open circles) with the calculated ones [77LV], in terms of spin-phonon coupling. According to this theory the change  $\Delta c_{ij}$  due to such interactions consists of first  $\Delta c_{ij}^{(1)}$  and second  $\Delta c_{ij}^{(2)}$  order contributions. Thus, the model associates this anomaly in elastic constant  $\Delta c_{11}$  as well as in its combination with  $\Delta c_{12}$  with the presence of first order spin phonon self energy only ( $\Delta c_{11} = kT^2$ ), where  $k$  is constant. Only second order interaction is present in  $\Delta c_{44}$  (see Fig. II.34). Note that at low temperatures a Holstein-Primakoff approximation (HPA) is hold while at temperatures close to  $T_N$  a chain-decoupling approximation (CDA) describes well a pronounced dip at  $T_{\min} \approx 47$  K, that lies 6 K below  $T_N$  ( $= 53$  K). Inset: the low temperature data on a log-log plot.

**Fig. II.37.** UN s.c. Elastic constants,  $c_{ij}$ , vs. temperature,  $T$ , [85YLGS]. These measurements agree within a few percent in the absolute value of the elastic constants with those of Ref. [77VD1] (see Fig. II.34), but show distinct differences in the paramagnetic region and in the vicinity of  $T_N = 53$  K. In the vicinity of  $T_N$  all elastic modes exhibited discontinuities being reminiscent of a structural phase transition, which has not been detected by [80KLMV] and detected by [75MSWK]. The elastic constants  $c_L = (c_{11} + c_{12} + 2c_{44})/2$  and  $c_B = (c_{11} + 2c_{12})/2$



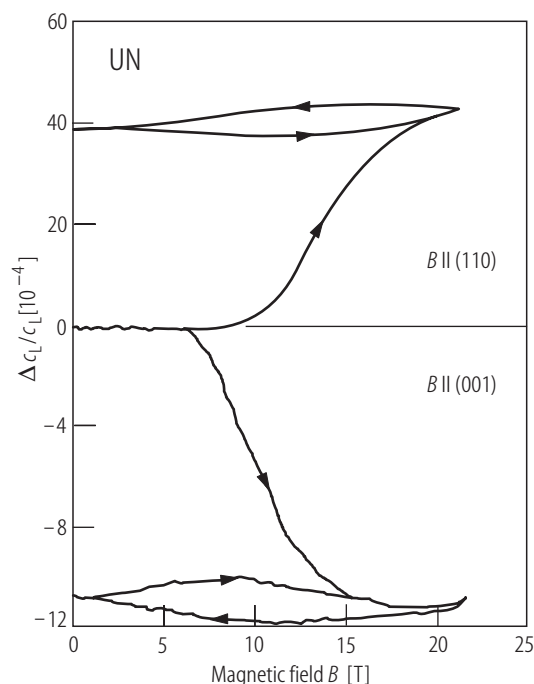


**Fig. II.38.** UN s.c. The longitudinal elastic constant,  $c_L = (c_{11} + c_{12} + 2c_{44})/2$ , vs. applied field,  $B$ , up to 22 T directed as indicated [90YS]. Note an anticlockwise hysteresis loop with the increase and decrease of the field along the [110] axis but a clockwise manner along the magnetic easy axis [001]. In the case of the transverse elastic constants  $c_{44}$  the behaviour is opposite.

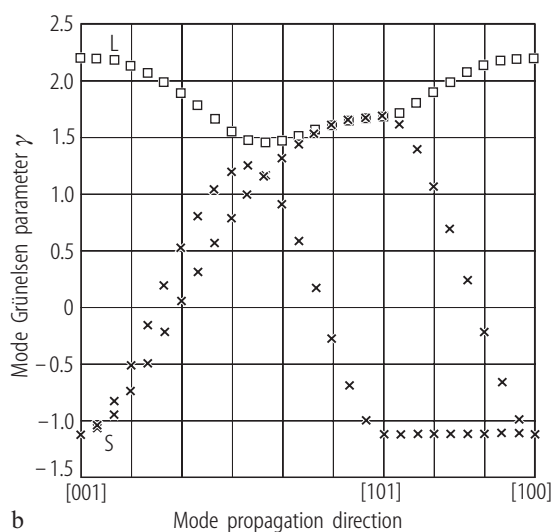
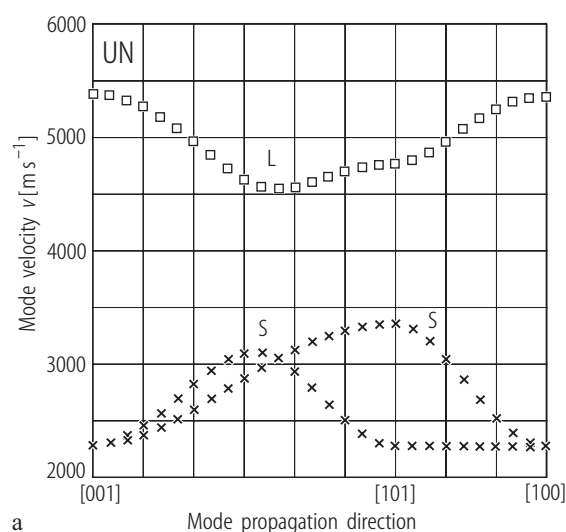


**Fig. II.39.** UN s.c. (a) The acoustic mode velocities, found by solution of the Christoffel equation as a function of mode propagation direction [86SMSD]. L and S mean longitudinal and shear modes that are polarized in the [001] and [110] directions and propagating in the [110] direction. For parameters see the Table below:

Elastic stiffness constants at 290 K		Volume compressibility $\kappa^S [10^{-12} \text{ m}^2 \text{ N}^{-1}]$	4.82±0.02
$c_{11} [10^{10} \text{ Nm}^{-2}]$	42.39 ±0.06	Linear compressibility $[10^{-12} \text{ m}^2 \text{ N}^{-1}]$	1.61
$c_{12}$	9.81±0.09	Debye temperature $\Theta_D^{\text{el}}$	282 K
$c_{44}$	7.57±0.02	Mean Grüneisen parameter $\gamma_H^{\text{el}}$	0.71
$c' (= 1/2(c_{11}-c_{12}))$	16.29±0.01	Thermal Grüneisen parameter $\gamma^{\text{th}}$	1.98
Anisotropy ratio $c'/c_{44}$	2.15	Bulk modulus $B_S [10^{10} \text{ Nm}^{-2}]$	20.67±0.08

(b) Mode Grüneisen parameter,  $\gamma(p,N)$ , in the long-wavelength limit as a function of mode propagation directions, L and S, as in figure (a) [86SMSD].

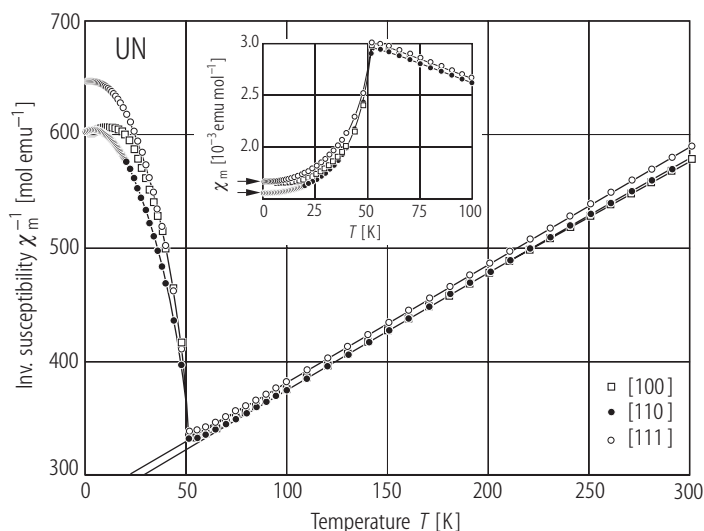


**Fig. II.40.** UN s.c. Inverse molar magnetic susceptibility,  $\chi_m^{-1}$ , vs. temperature,  $T$ , measured along three main crystallographic axes [05DTSM]. For all these directions the average values of  $\Theta = -249$  K and  $p_{\text{eff}} = 2.65 \mu_B$ . Inset:  $\chi_m$  vs  $T$  around  $T_N (= 51.5$  K). The arrows give the susceptibility values found from the slope of the  $\sigma$  vs.  $H$  straight lines at 1.9 K.

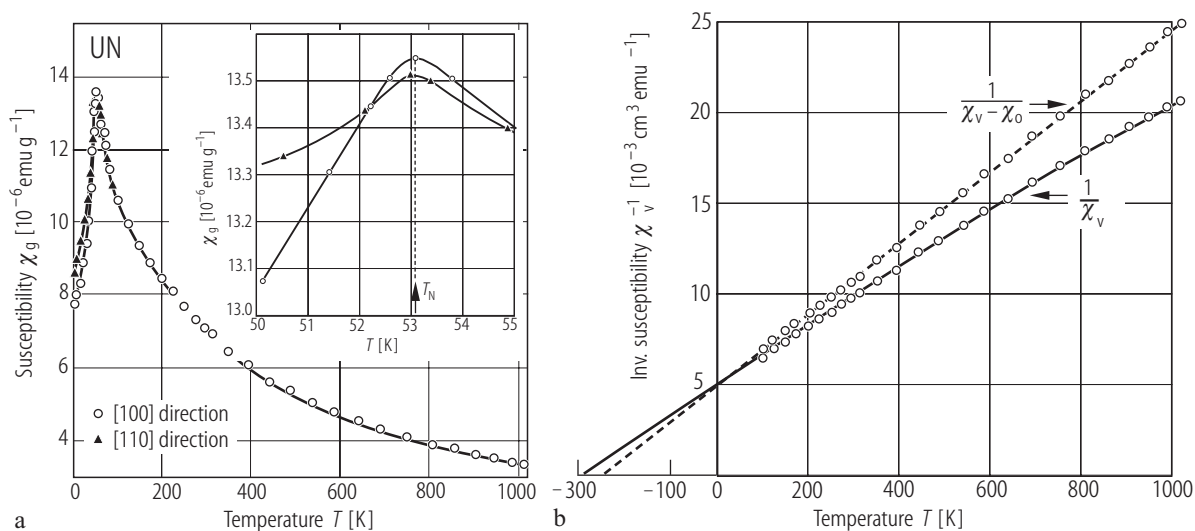


**Fig. II.41.** UN s.c. **(a)** Specific magnetic susceptibility,  $\chi_g$ , measured between 4...1000 K along the [100] direction and between 4 and 100 K along the [110] direction. The inset shows the  $\chi_g$  vs.  $T$  dependence for these two directions around  $T_N$  [77VD2].  $T_N = 53.1(2)$  K. **(b)** Inverse volume magnetic susceptibility,  $\chi_v^{-1}$  and  $(\chi_v - \chi_0)^{-1}$ , vs. temperature,  $T$ , measured up to 1000 K [77VD2]. The results were also presented in Fig. 3 and 4 in LB III/12c, p.420 (1981). For comparison of the magnetic parameters obtained by different authors see the Table below.

	Temp. range [K]	$\chi_0$ [ $10^{-6}$ emu/mol]	$\Theta_p$ [K]	$p_{\text{eff}}$ [ $\mu_B$ ]	$T_N$ [K]	Reference
1	83...290	—	−310	3.08	—	62TTL
2	100...300	—	−325	3.11	—	64AJD
3*	60...550	500	−160	2.06	52	*69RD2
4	$T < 600$	—	−247	2.93	52	72ONK
	$T > 600$	—	−383	3.20	—	
5	$T < 500$	—	−250	2.93	53(1)	75T
	75...1000	21.7	−200	2.50		
6	100...500	—	−292	2.83	53.1(2)	77VD2
s.c.	100...1000	8	−247	2.66		

\*These data are affected by the presence of 2000 ppm of carbon – see [72DC]. See also [70MFM] and [71K].

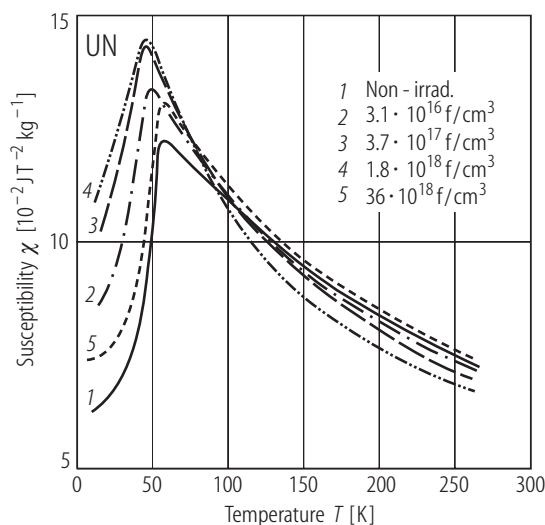


**Fig. II.42.** UN (fused). Magnetic susceptibility,  $\chi$  (in  $\text{J/T}^2\text{kg}$  units), vs. temperature,  $T$ , for neutron irradiated and non-irradiated samples [83MTKN]. The recovery of the behaviour for the sample (5) with the highest used fission dose is not understandable. Note that  $T_N$  for sample (4) decreases down to about 40 K (about 20%) in relation to the non-irradiated sample (1).

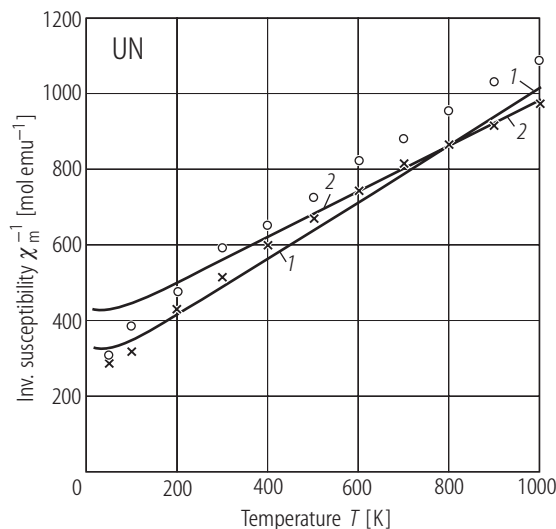


**Fig. II.43.** UN. Calculation of  $\chi_m^{-1}$  according to the equation:  $\chi_m = \chi_0 / (1 - \lambda\chi_0)$ , where  $\chi_0$  is the absence of molecular field and  $\lambda$  is a modified molecular field coefficient [78LL2]. The calculations of curves 1 and 2 by using different parameters (see the original paper) are fitted to two experimental data of [75T] (crosses) and [69RD2] (open circles), respectively. A model with  $\text{U}^{4+}$  ( $5f^2$ ) has been assumed. The ordered moment ( $p_0 \approx 0.75 \mu_B/\text{U at.}$ ) is accounted for in terms of a simple two-level model.

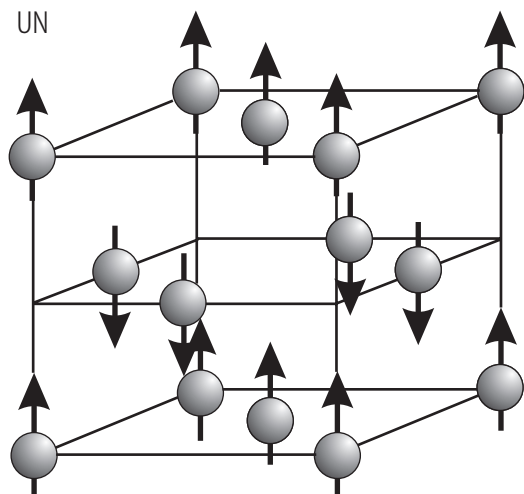


**Fig. II.44.** UN (GdN). Magnetic structure, with magnetic moments along [001], first determined as AF I-type [65C] and then as a single- $k$  one [80RBQV].  $T_N = 53 \text{ K}$ ,  $p_0 = 0.75 \mu_B/\text{U at.}$  Compare the opposite magnetic behaviour with the presence of oxygen (increase in  $T_N$ ) and carbon (rapid decrease in  $T_N$ ) impurities in UN with respect to those in ferromagnetic GdN ( $T_C \sim 70 \text{ K}$ ) [71K].

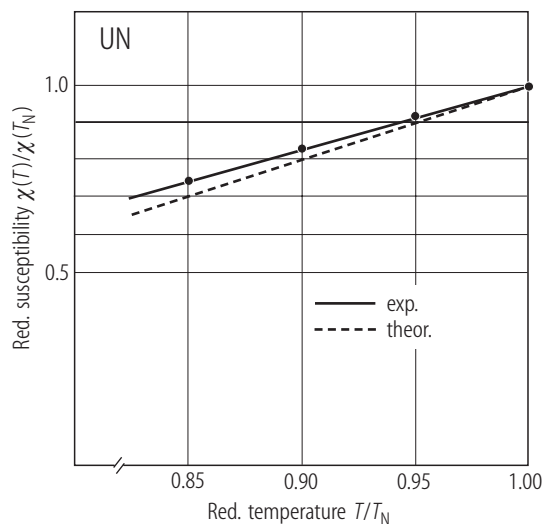
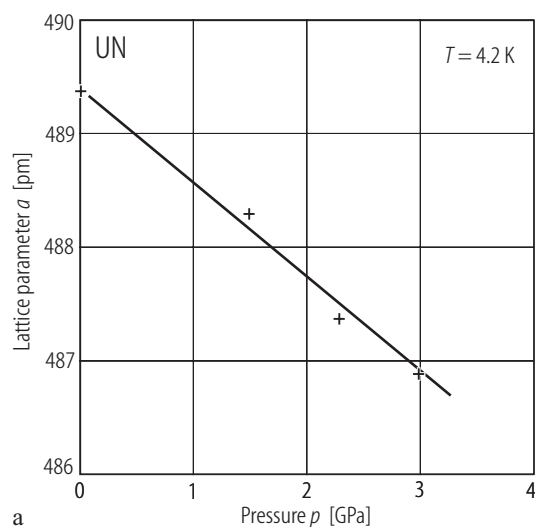
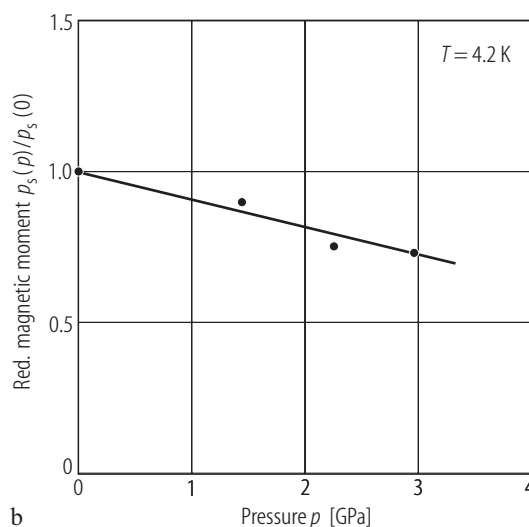


**Fig. II.46.** UN (sintered). Reduced magnetic susceptibility,  $\chi(T)/\chi(T_N)$ , vs. reduced temperature,  $T/T_N$  [79FBD]. Note a comparison with theoretical prediction for an itinerant antiferromagnet that  $\chi(T)$  should be linear just below  $T_N$  following the expression:  $\chi(T) = \chi(T_N)[1 - A(1 - T/T_N)]$ , where  $A^{\text{theor}} = 2$ ,  $A^{\text{exp}} = 1.74$ .

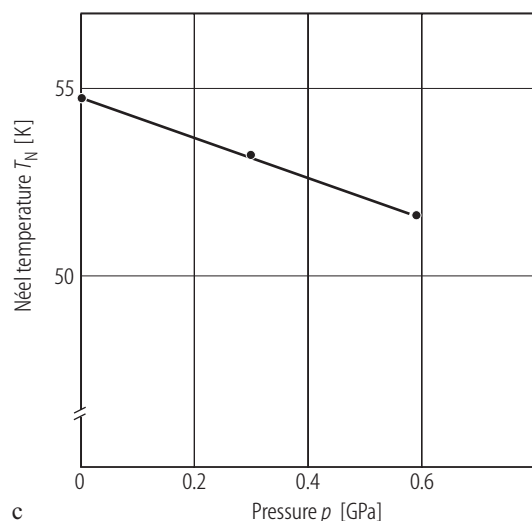
For Fig. II.45 see next page



a



b



c

**Fig. II.45.** UN. (a) The lattice parameter,  $a$ , vs. pressure,  $p$ , up to 3 GPa at 4.2 K [80FBBV]. The compressibility  $\kappa = 0.5 \text{ (Mbar)}^{-1}$ . (b) The reduced value of the ordered moment,  $p_s(p)/p_s(0)$ , vs. pressure,  $p$ , up to 3 GPa [80FBBV]. In this range of pressure  $p_s(p)$  is reduced from  $0.75 \mu_B$  to  $0.54 \mu_B$ ;  $d \log p_s / dp = -10 \text{ (Mbar)}^{-1}$ . (c) The Néel temperature,  $T_N$ , vs. pressure up to 0.6 GPa [79FBD];  $d \log T_N / dp = -10 \text{ (Mbar)}^{-1}$ . Note that  $T_N$  and  $p_s$  have the same volume dependence:  $d \log T_N / d \log V = d \log p_s / d \log V = 19$ . This is taken as experimental evidence of a band antiferromagnetism in UN.

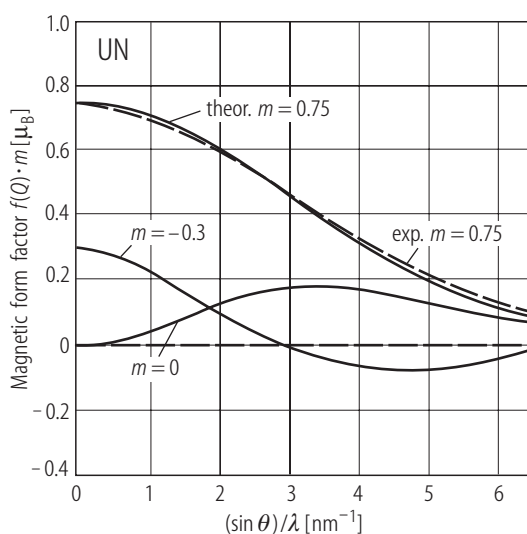


**Fig. II.47.** UN. Calculated magnetic form factor  $f(Q)$  for various values of the total moment,  $m$ , vs. scattering vector  $Q/4\pi (= \sin \theta / \lambda)$  [83BK] and [93B1]. The variation in values of magnetic moments in calculation results from the quenching under pressure of the orbital moment content. The total moment is expected to go through zero, due to the antiparallel arrangement of the spin ( $m_S$ ) and orbital ( $m_L$ ) contributions at ambient pressure, where  $m_L > m_S$  and more rapidly change with pressure of  $m_L$  than  $m_S$ . This is expected to occur in a number of actinide compounds when such studies under pressure will be done.

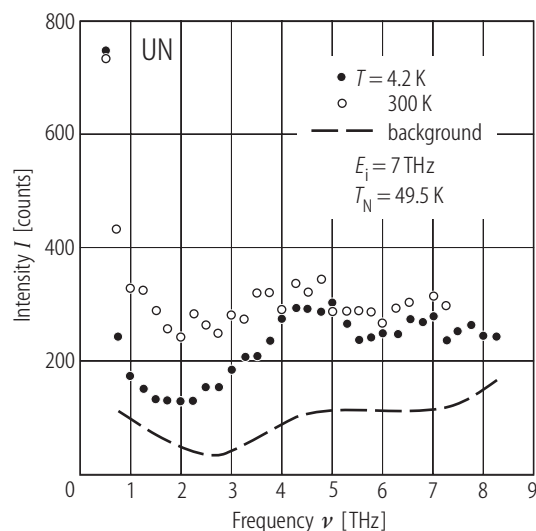


**Fig. II.48.** UN s.c. Inelastic neutron scattering (INS) intensity,  $I$ , as a function of frequency,  $\nu$ , at the ordering wavevector at two temperatures 4.2 and 300 K [83BHJM]. The dashed curve gives an estimate of the background scattering. The magnetic response at the (110) magnetic rlp is a broad (FWHM = 5(1) THz) distribution of intensity, peaked at 4.2(5) THz. The symmetry of the magnetic response is primarily longitudinal. Note that the paramagnetic scattering is larger in intensity at all frequencies than the lower temperature response. Though UN presents a large negative Curie-Weiss constant ( $\Theta_p \approx -200$  K), there are unequivocal strong ferromagnetic fluctuations.

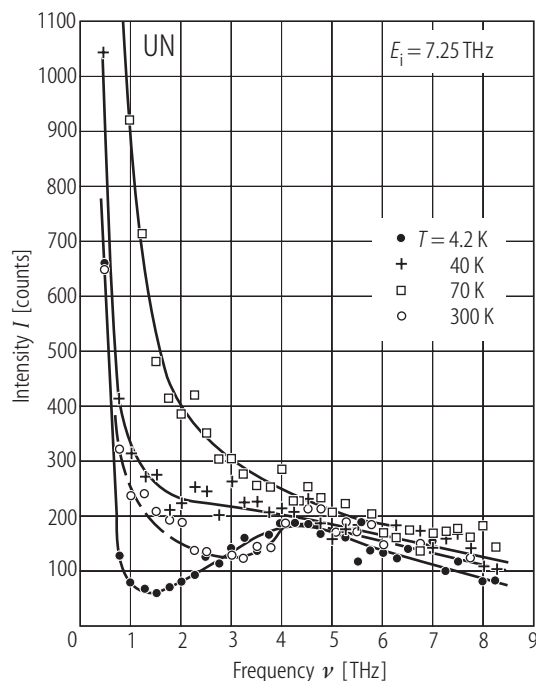


**Fig. II.49.** UN s.c. The inelastic scattering intensity,  $I$ , at the magnetic reciprocal lattice point (110), corrected with background, taken at four temperatures (indicated) as a function of frequency transfer  $\nu$  [80BMHS]. Note that the scattering intensity grows rapidly as the temperature is raised in the ordered phase. It is clear that the observed response must be associated with the transitions within the 5f - 6d band near  $E_F$ . The results indicate a steeply rising branch of excitation with an anisotropy gap. This is the first direct experimental evidence for high-velocity longitudinal spin excitation in magnetically ordered actinide compounds [79HSBL].

For Fig. II.50 see next page

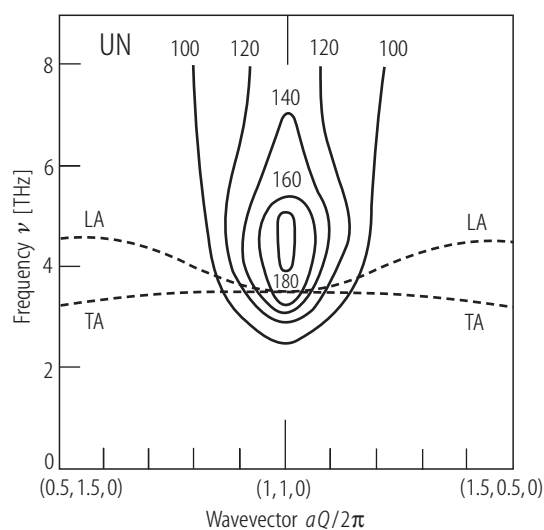


**Fig. II.51.** UN s.c. Contours of constant magnetic scattering intensity at 4.2 K obtained in a series of constant- $Q$  and constant- $\nu$  scans in the vicinity of (110) [80BMHS], [82HBSL]. The dashed curves represent the dispersion relation for longitudinal (LA) and transverse (TA) acoustic phonons. Note that the maximum magnetic scattering in UN occurs just in the frequency range of the maximum acoustic mode frequencies (see [78DHSB] and Fig. II.33). This type of locking suggests that the lattice vibrations may play a role in the uranium pnictide series in a similar way to that as in the mixed-valence mechanism discussed by [74GE].

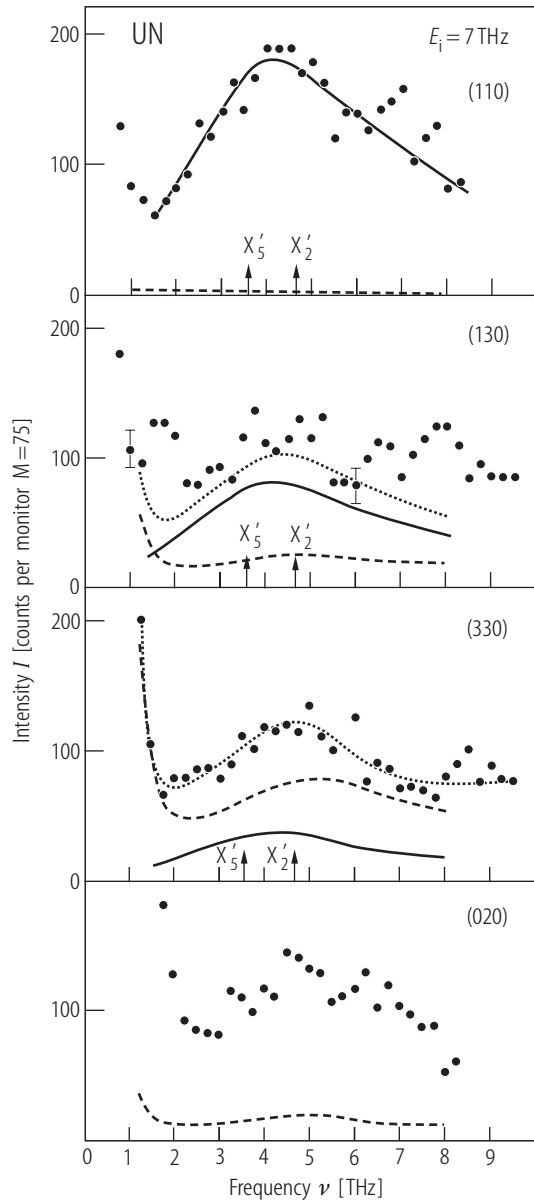


**Fig. II.50.** UN s.c. The distribution of scattered neutrons at 4.2 K for constant- $Q$  scans at (110), (130), (330) and (020) as a function of frequency,  $\nu$ , corrected for the sample-out background and normalized to the same number of incident neutrons [84HBSL]. Note a broad magnetic distribution with a maximum around 4.5 THz, which decreases in intensity as the wavevector  $Q$  increases (solid curves). There is apparent locking of this magnetic response to the region of maximum phonon frequency at X. The scattering at (110) is completely magnetic in character. However, the absence of any well-defined collective spin-wave modes is the most surprising feature. The dashed curves denote two-phonon scattering, and the dotted curve denotes the sum of magnetic and phonon contributions, while direct coherent one-phonon scattering is negligible. The arrows mark the frequencies of the  $X'_5$  and  $X'_2$  modes (see Fig. II.33).

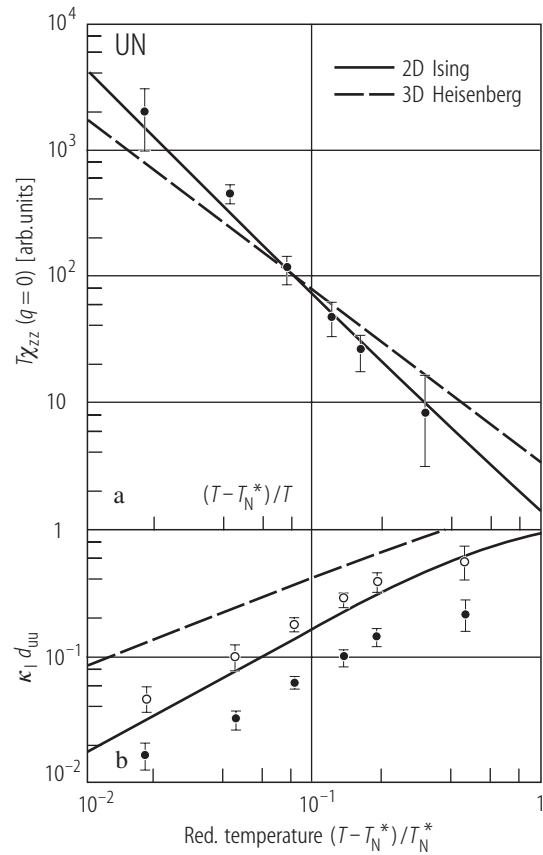


**Fig. II.52.** UN s.c. (a) The parallel susceptibility,  $\chi_{zz}$ , measured at (110) times the temperature  $T$  vs. reduced temperature [80BMHS]. This is compared to 2D-Ising (solid line) and 3D-Heisenberg (dashed line) behaviour. (b) Inverse correlation range of spin fluctuations parallel,  $\kappa_{||}$ , (open circles) and perpendicular,  $\kappa_{\perp}$ , (closed circles) to (0,0,1) times the nn U-U distance ( $d_{UU} \approx 0.345$  nm) as a function of reduced temperature [82HBSL]. Both dependences are drawn in double logarithmic scales. Note that neutron critical scattering shows a marked anisotropy expressed by the ratio  $R = \kappa_{||}/\kappa_{\perp} = 2.8(3)$ , which indicates that the spin correlations are thus quasi-two-dimensional, i.e. the spins are highly correlated within each (001) sheets. – For both above dependencies,  $T_N$  was determined as the temperature at which the measured correlation ranges tend to infinity, i.e.  $T_N^* = 54.5$  K (see Fig. II.53b). This leads to some difference in the same dependencies, presented in [78BHSL], where  $T_N (= 49.5(3)$  K) was taken from the disappearance of the magnetization. Probably between  $T_N$  and  $T_N^*$  is a complex region, where the correlations between spins are becoming more three-dimensional in character.

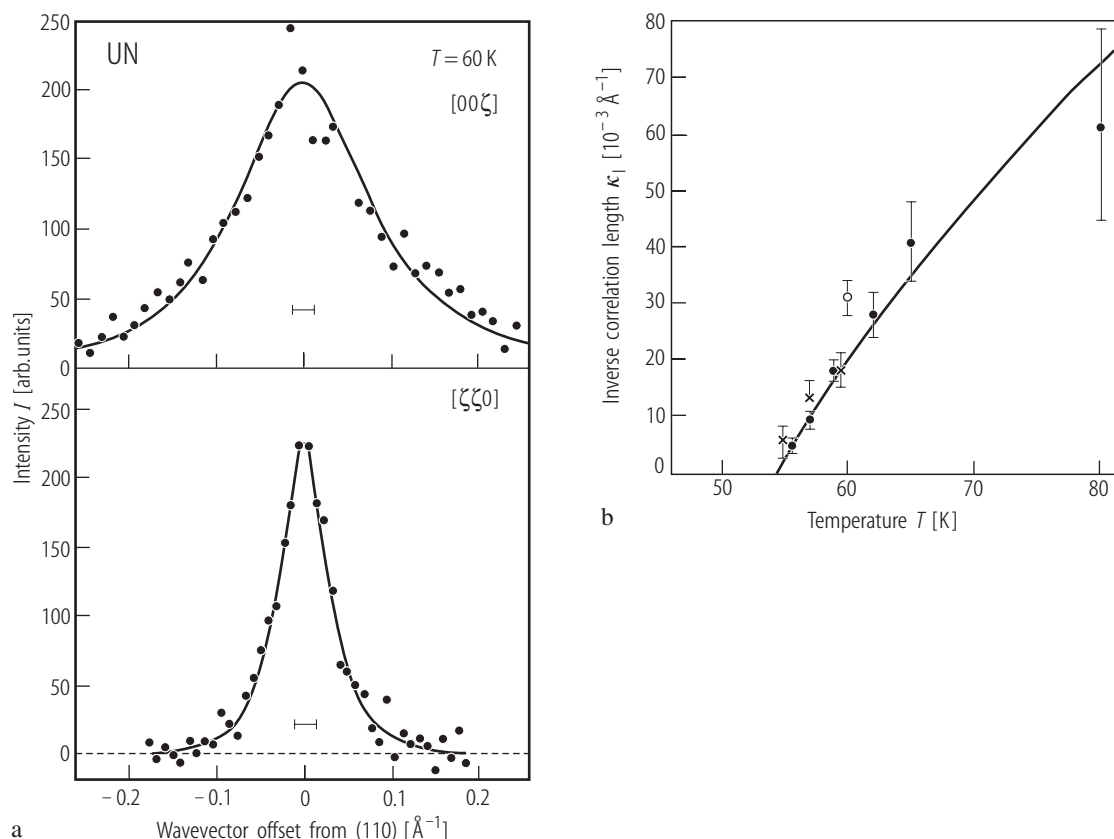


**Fig. II.53.** UN s.c. **(a)** Anisotropy of critical scattering at 60 K ( $T > T_N$ ) taken from the (110) magnetic reciprocal lattice point in the  $[00\zeta]$  and  $[\zeta\zeta 0]$  directions and for zero-frequency transfer [82HBSL]. Note a ratio of about 3:1 in the width of the peaks. The solid lines represent least-squares fits of the data to the dynamical susceptibility. The anisotropic exchange model describes the interactions between  $z$  components of spins that are strong for the four near neighbours within (001) sheets and weaker for neighbours between the (001) planes. **(b)** Inverse correlation length  $\kappa_1$  vs. temperature for critical fluctuations in the  $[100]$  direction [82HBSL]. The closed circles are two-axis (spectrometer) data. The results (see the text) at 55, 57,

59 K (crosses) and at 60 K (open circle) were made by integrating triple-axis (spectrometer) data. The latter point was determined under different resolution conditions. The solid line represents a least-squares fit to the equation  $\kappa_1 = 0.14(2)[(T - T_N^*)/T_N^*]^{0.84(5)}$  with an associated exponent  $\nu = 0.84(5)$  and  $T_N^* = 54.5 \text{ K}$  found by extrapolation of  $\nu$  to  $\kappa_1 = 0$ . The determined exponent is close to that for the two-dimensional 2D Ising model ( $\nu = 1$ ) for the temperature range  $T > T_N + 4 \text{ K}$  ( $T_N = 49.5(5) \text{ K}$ ). This is interpreted in terms of strong correlations within (001) planes with weak correlations between these planes. For the 3D Heisenberg model  $\nu = 0.70$ .



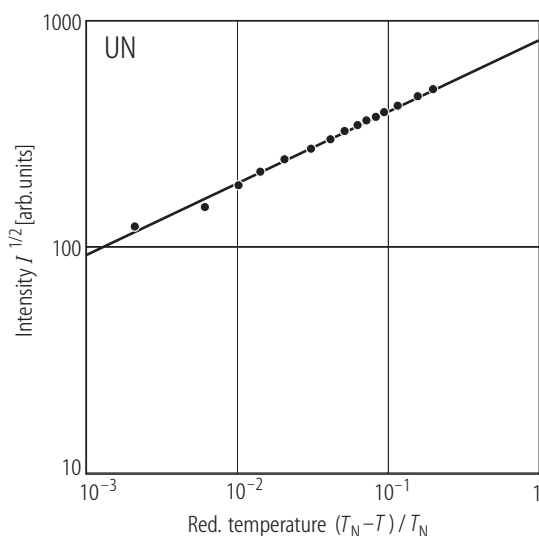


**Fig. II.54.** UN s.c. The square root of the Bragg peak intensity  $I$  in the ordered phase vs. reduced temperature  $(T_N - T)/T_N$  on a log-log scale [82HBSL].  $T_N = 49.5(5)$  K (note that this temperature is lower than other reported values). The order parameter  $\beta = 0.31(3)$  is characteristic of a three-dimensional magnetic material.

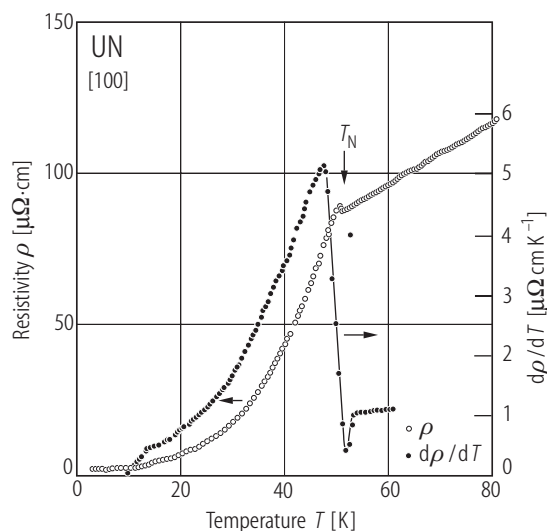
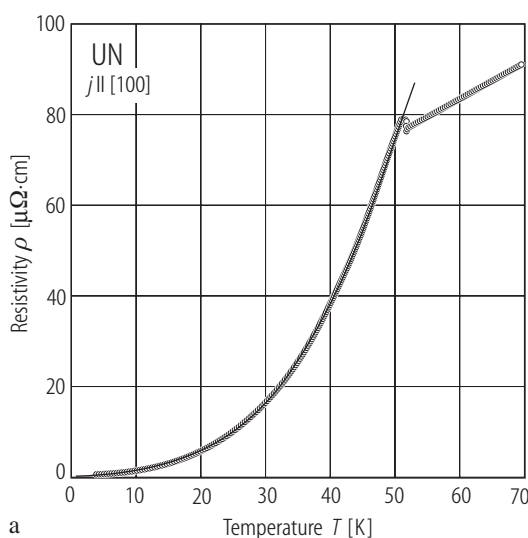
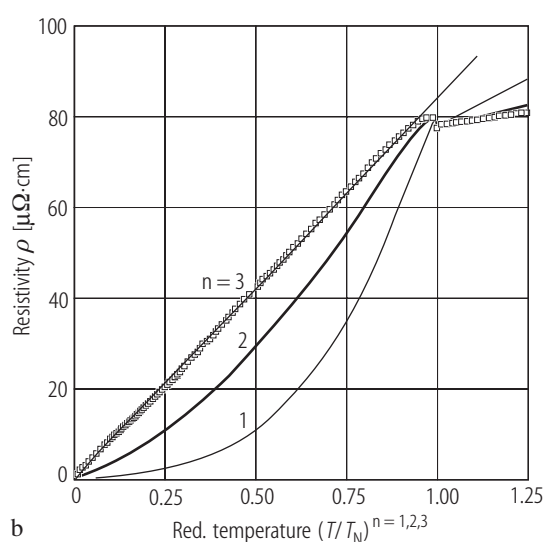


**Fig. II.55.** UN s.c. [100]. Low-temperature dependencies of the resistivity,  $\rho$ , and the derivative  $d\rho/dT$  vs.  $T$  [76NKMT].  $T_N = 50.5$  K. Compare this behaviour with the data of [77DV] presented in Figs. 5 and 6 in LB III/12c, p.420 (1981). In both cases a small hump below  $T_N$  was observed which seems not to be caused by the change in Brillouin zone volume due to the magnetic order. This is because the crystallographic and magnetic unit cells have the same size [65C]. Another possibility is the formation of a gap at  $E_F$  in the electronic structure due to an itinerant antiferromagnetism [79FBD].



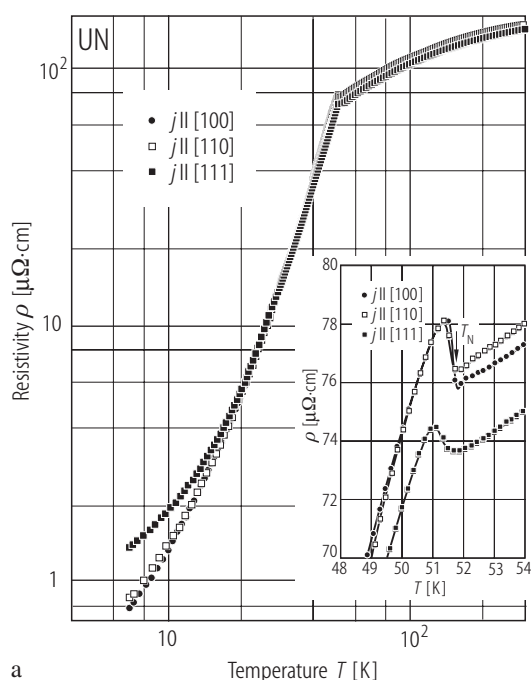
a



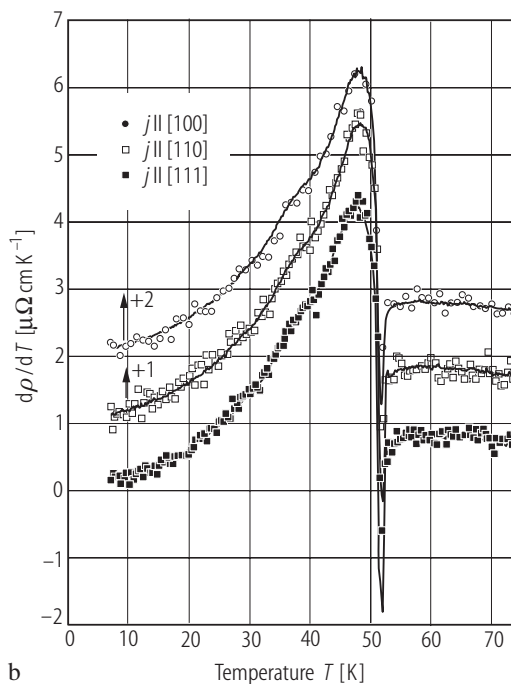
b

**Fig. II.56.** UN s.c. (a) Electrical resistivity,  $\rho$ , vs. temperature,  $T$ , data obtained in the configuration  $j \parallel [100]$  and fitted to the formula  $\rho = \rho_0 + AT^2 + BT(1 + 2T/\Delta)\exp(-\Delta/T)$  appropriate for an energy gap ( $\Delta$ ) in antiferromagnets with an additional  $T^2$  term manifesting the Fermi-liquid behaviour (solid line) [05DTSM]. (Fit at  $4 \text{ K} < T < 40 \text{ K}$ ,  $\rho_0 = 0.2 \mu\Omega\text{cm}$ ,  $A = 0.013 \mu\Omega\text{cm/K}$ ,  $B = 652 \mu\Omega\text{cm/K}$ ,  $\Delta = 162 \text{ K}$ ).

(b) Low-temperature data of electrical resistivity,  $\rho$ , plotted against  $(T/T_N)^n$  ( $n = 1, 2$  and  $3$ );  $T_N = 51.7 \text{ K}$  [05DTSM]. An exact straight-line behaviour is obtained for  $n = 3$  in agreement with the s.c. data of [76NKMT] and somewhat different from  $T^{2.38}$  given for sintered sample and presented in Fig. II.62.



a



b

**Fig. II.57.** UN s.c. **(a)** Electrical resistivity,  $\rho$ , vs. temperature,  $T$ , on double logarithmic plot, measured along three main crystallographic directions [05DTSM]. Inset:  $\rho$  vs.  $T$  around  $T_N$ . Note a hump in  $\rho(T)$  observed just below  $T_N$  ( $= 51.7(2)$  K) in all three cases. This confirms earlier results of [76NKMT] and [77DV]. **(b)** Temperature

derivative of the resistivity,  $d\rho/dT$ , vs. temperature,  $T$ , inferred for three main crystallographic directions [05DTSM]. Note a sharp minimum in this dependence just at  $T_N$  ( $= 51.7$  K). The curves are shifted up for  $j \parallel [110]$  and [111].

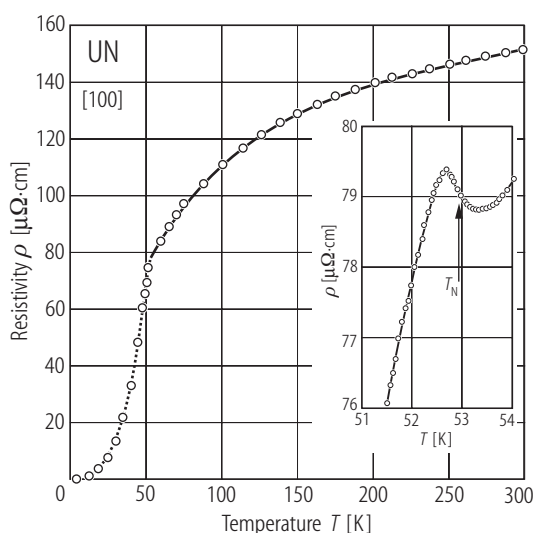


**Fig. II.58.** UN s.c. Electrical resistivity,  $\rho$ , vs. temperature,  $T$ , measured along the [100] direction after subtraction of the residual resistivity  $\rho_0$  ( $= 1.18 \mu\Omega\text{cm}$ ) at 4 K [77DV]. The dotted line demonstrates that the spin-disorder resistivity is proportional to  $(1-m^2)$  ( $m$  is the reduced sublattice magnetization taken from [65C]).  $T_N = 51.7$  K. The inset shows the  $\rho$  vs.  $T$  variation around  $T_N$  ( $= 53$  K). A small peak observed below  $T_N$  could be the effect either of the formation e.g. of a spin -density wave (SDW)-like magnetic order or a new Brillouin zone boundary arisen probably due to an antiferromagnetic ordering [63EW], but of somehow different type than that reported in the literature. As was reported [65C], there is no change in the volume of chemical and magnetic unit cells which should leave the BZ unchanged. For discussion of this problem see also [77VD3].